Mechanics of Cilia Beating

Quantifying the behaviours that define effective cilia driven fluid flow

By

JON HALL

The University Of Sheffield.

Department of Physics and Astronomy
UNIVERSITY OF SHEFFIELD

A dissertation submitted to the University of Sheffield in accordance with the requirements of the degree of DOCTOR OF PHILOSOPHY in the Faculty of Physics and Astronomy.

JULY 2020

Word count: 28,386

Abstract

This thesis explores the mechanical properties of cilia driven fluid flow through computer simulations of cilia interacting with fluid. First of all we look at the effect of a single beating cilium on a large fluid region by examining the fluid velocity profiles associated with the resulting fluid flow. From these results we are able to quantify the observed velocity profile using a characteristic length, and show the relationship between this characteristic length and the Reynolds number. We go on to investigate the relationship between the metachronal wavelength of an array of beating cilia and the resulting fluid flow rate. We find that the observed relationship is well described by the clustering of cilia during the active stroke, and we quantify this by deriving an analytical model of the free area in the cilium array which depends on the metachronal wavelength. We show that there is a strong correlation between our analytical model and simulation results, which implies that the changes in fluid flow rate linked to a change in free area. Next we look at the differences in fluid flow with and without metachrony for a large array of cilia, concluding that the increase of fluid flow rate due to metachrony is greater when the space between cilia is reduced. Finally we investigate the effect of de-ciliated regions on fluid flow by simulating several arrangements of ciliated and de-ciliated cells. Results from these simulations show that the arrangement of de-ciliated cells can affect fluid flow by increasing the distance between active wave fronts, which in turn causes the coordination between cilia to be less effective.

Dedication and acknowledgements

I would like to dedicate this thesis to my parents, José and Peter. They will be more excited than anyone else to call me “Doctor Hall”.

I would like to thank my supervisor Prof. Nigel Clarke for all of his ideas and guidence. I would also like to thank Dr. Rhoda Hawkins and Dr. Paul Richmond for all of their support throughout this work.

AUTHOR'S DECLARATION

I declare that the work in this dissertation was carried out in accordance with the requirements of the University's Regulations and Code of Practice for Research Degree Programmes and that it has not been submitted for any other academic award. Except where indicated by specific reference in the text, the work is the candidate's own work. Work done in collaboration with, or with the assistance of, others, is indicated as such. Any views expressed in the dissertation are those of the author.

SIGNED: ..... DATE: .....

Table of Contents

List of Tables

Table **Page**

List of Figures

Figure **Page**

Preface

Motile cilia are present in many different locations within the human body; inside the lungs, brain, and in both the male and female reproductive systems. Cilia themselves are long thin filaments that extend from the surface of cells to interact with fluids. Within the lungs and ovarian tubes ciliated cells line the walls of mucus membranes. The cilia attached to these cells beat steadily to transport particles and cells within the mucus. Muco-ciliary transport is a vital process that prevents infection and blockages in the lungs. This process is very sensitive to changes in the rheology of the mucus and the coordination of motile cilia beating. Because of this there have been numerous studies, both experimental and theoretical, focused on understanding the key parameters muco-ciliary transport.

The aim of our work is to quantify the parameters and mechanics that contribute to effective cilia driven fluid flow using a combination of numerical and analytical modelling. We investigate exactly how changes to cilia spacing, fluid rheology, metachronal wavelength, and arrangement of ciliated cells affect muco-ciliary transport through computational simulations. We also use results from these simulations to construct an analytical model of an array of beating cilia to quantify some of the behaviours that we observe.

We begin in by giving a review of previous work in this field that has been instrumental in the development of our model and used as a basis for our own work in chapter 1. We then describe the computational methods that we have used to build our model in chapter 2, along with some preliminary results that we have used as a benchmark for our numerical model. In chapter 3 we present the results of an investigation into fluid flow generated by a single beating cilium, and the velocity profiles that this generates in the fluid. Chapter 4 describes a study of the relationship between metachrony and fluid flow rate, in which we use an analytical model to quantify the clustering of cilia beating in a metachronal wave. In chapter 5 we present results from two investigations where we have applied our computational model to quantify the effects of cilium spacing and de-ciliated regions on fluid flow. And finally in chapter 6 we summarise and discuss the results of our work, and suggest directions for future work in this area.

1

BACKGROUND

In this chapter we provide a review of the existing literature in the field of cilia driven fluid flow. We begin by identifying the properties of pulmonary cilia and muco-ciliary clearance that have been observed through electron microscopy and high speed imaging [7, 26, 41, 43, 44]. This includes information on the internal structure of the cilium and how this dictates the shape of the cilium beat profile [7, 44–46].

We give a comprehensive definition of metachrony and its importance for effective cilia driven fluid flow. This ranges from the earliest in vitro observations of metachrony in pulmonary cilia [39] to recent simulation results investigating some of the intrinsic properties of cilia beating with a metachronal wave [22, 24]. We pay particular attention to simulation work investigating how metachrony and the metachronal wavelength affect the rate of fluid flow generated by an array of beating cilia [6, 11, 24].

We present results from Chatelin and Poncet [7] that highlight the important fluid properties for effective cilia driven flow. The properties that we see as most important for our work are the depth of the peri-ciliary liquid (PCL) relative to the cilium length, the stiffness of the transition between the PCL and the mucus, and the viscosity ratio between the PCL and the mucus. We also describe the peri-ciliary brush model proposed by Button et al. [5], and how the presence of mucin strands between cilia contributes to the separation of the PCL and the mucus layer.

We describe the mechanics of mucin hydration as described by Sircar and Roberts [43], and how this relates to the kinetics of swelling gels derived by Keener et al. [25]. We also describe the process of mucin secretion from goblet cells and how these mucins form the mucus layer [47].

Finally we describe some of the disease states that can affect cilia beating and muco-ciliary clearance. We look at Asthma, cystic fibrosis, and chronic obstructive pulmonary disease (COPD) to highlight whether the symptoms of these diseases affect the cilia themselves or the rheology of the mucus in the lungs [1, 12, 17, 37, 42].

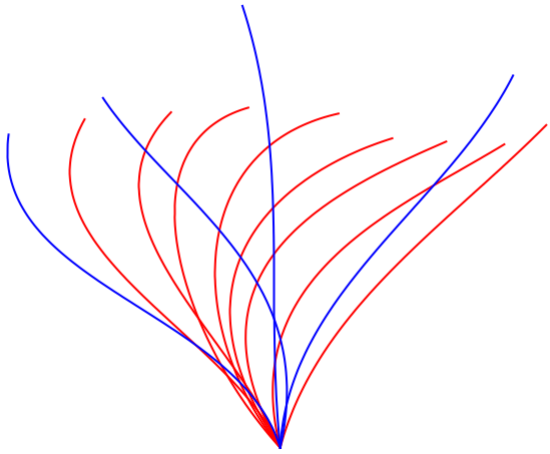

Figure 1.1: A superposition of the beat profile for pulmonary cilia as observed by Fulford and Blake [14].

1.1 Pulmonary Cilia

Pulmonary cilia form a dense mat which lines the trachea and bronchial tubes, pertruding between five and seven microns from the epithelial surface [44]. The cilia are immersed in a fluid that is separated into two distinct layers. The fluid in the lower layer is essentially water, and is referred to as peri-cilliary liquid (PCL) [7, 41, 44]. The upper layer is a visco-elastic fluid made up of cross-linked polymers called mucins. The mucins originate from the epithelium and travel through the PCL to form the upper layer of mucus, at a height of around six microns from the epithelium [7, 26, 43]. Cilia beat in an asymmetric pattern with an active stroke and a recovery stroke [44], a superposition of this beat profile is shown in Fig. 1.1. The active stroke is a planar motion with the cilium remaining virtually straight throughout and rotating about its base. During the recovery stroke, the cilium bends and moves in the opposite direction while also rotating out of the plane of the active stroke. This asymmetric motion means that the work done by the active stroke is greater than that done by the recovery stroke, causing a net fluid flow in the direction of the active stroke [44].

1.1.1 Cilium Internal Structure

It has been acknowledged in many articles written on this topic that the internal structure of a cilium must be modelled in order to fully understand the complexities of cilia beating [7, 44–46]. The reasoning behind this is that by controlling the forces acting within a cilium rather than the beat profile of the cilium it is possible to directly observe the effects of the surrounding fluid on the cilium [16, 34, 51]. This would provide a closed loop simulation of how cilia beating affects fluid flow and vise versa.

The internal structure of a motile cilium is formed of 9 microtubules arranged in a circle

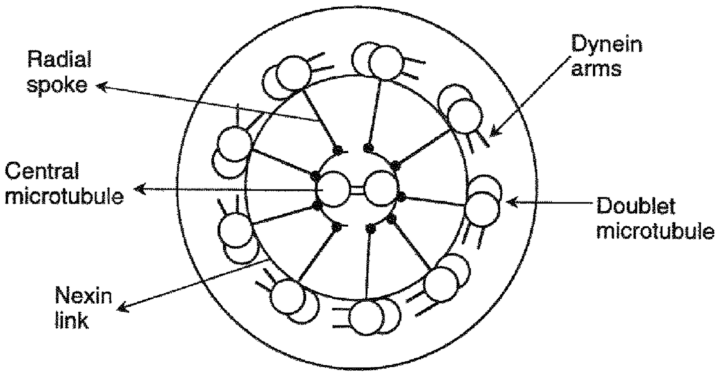

Figure 1.2: The cross section of a cilium, showing the internal structure of microtubules. Graphic reproduced with permission from Yang et al. (2008) [51].

around the edge of the cilium cross section, with an additional 2 microtubules in the centre as shown in figure 1.2. The circle of microtubules are connected to one another by nexin strands, and each one is connected to the central pair by a radial spoke. These elements have been shown to behave like elastic strings [34, 51]. Dynein motors exert a force on neighbouring microtubules to make them move in a sliding motion relative to one another. The movement and bending of a cilium are the result of the forces acting on the microtubules in a specific sequence [40] combined with the passive spring forces from the nexin strands.

In the simulations of Mitran [34] this internal structure was modelled relatively simply by approximating microtubules as thin walled beams made up of 20 beam elements that are acted on by forces and springs representing the dynein motors and nexin strands respectively. The dynein forces were coordinated based on experimental data to produce a planar motion representative of the three dimensional cilia beat strokes. The deformation of each cilium was calculated on a local body-fitted grid that interacts with a background Cartesian grid to transmit forces between the cilia according to the modelled properties of the surrounding fluid [34]. It should be noted that although the internal structure of the cilium and surrounding fluid were modelled in three dimensions, the beating pattern used in these simulations was strictly planar.

In these simulations each cilium started with an initial random phase, so that the cilia were not initially synchronised with one another. At each time step the internal phase of each cilium was adjusted to reduce the work done by that cilium against the surrounding fluid. Allowing the motion of a cilium to adapt in this way resulted in the synchronisation of cilia over large distances. More specifically a fixed phase difference between neighbouring cilia arose from hydrodynamic forces, resulting in the formation of a metachronal wave over large distances [34]. We discuss metachronal waves further in section 1.1.2.

In the work of Yang et al. [51], a two dimensional model of the cilium internal structure was used to investigate the effect of cilia coordination on muco-ciliary transport. The cilium structure in this model consisted of two microtubules connected by horizontal springs that represented nexin strands [51]. The dynein motors were represented as diagonal force vectors acting in

tangential directions for the active and recovery strokes. When the dynein motors contracted they caused the cilium to bend and through coordinated switching of the active and recovery forces, a beating pattern was achieved. The more complex form of the recovery stroke was controlled by a bending algorithm that activated dynein motors based on the local curvature of the cilium [51].

The force based model used in these simulations allowed for the cilium beat profile to be altered by hydrodynamic forces acting on the cilium from either the surrounding visco-elastic fluid or neighbouring cilia. This resulted in changes to the beat frequency and motion profile of coordinated cilia depending on the number of cilia and their relative positions. The results from this study showed that two cilia in close proximity would synchronise rapidly, and that cilia positioned further apart would exhibit metachronal behaviour [51]. A similar model created by Gueron et al. has shown the same behaviour on a larger scale, simulating ten to one hundred cilia [16]. The results from these simulations were also in agreement with simulation results from Mitran [34]. The simulations showed that, relative to a single cilium, two coordinated cilia would beat with a frequency that was 25% higher, and achieve a fluid flow rate that is 59% higher. The addition of a third cilium resulted in a frequency increase of less than 2%, and a flow rate increase of 20%. Increasing the viscosity of the surrounding fluid had the effect of decreasing the cilia beat frequency, in agreement with experimental findings [33].

1.1.2 Metachrony

Metachrony is characterised by a fixed phase difference between neighbouring cilia resulting in the propagation of the "effective region" [22], and has been evident since the earliest observations of cilia [39]. More recent work focused on the simulation of cilia beating and the dynamics of the surrounding fluids has shown that metachrony is vital for the efficient transport of visco-elastic fluids such as mucus [22, 51]. Results from modelling both the internal and external forces acting on a beating cilium imply that metachronal waves are caused by the hydrodynamic coupling between neighbouring cilia [16, 34], as discussed in section 1.1.1.

In the work of Hussong et al. [22] simulations were carried out to investigate the effects of metachrony alone, excluding the complex cilium beat profile. This was done by modelling an array of beating cilia as a deforming porous layer immersed in a viscous fluid. The deformation of the porous layer was representative of an array of straight cylinders that periodically rotated in a planar motion about their base. Due to the symmetry of the cilia beat pattern used in this model any net fluid flow could be attributed to the metachronal coordination of the system [22]. During the investigation the Reynolds number (Re) of the surrounding fluid was varied between 0.001 and 3500 to show the difference in behaviour between the viscosity and inertia dominated regimes.

The first thing that was apparent from the results of the low Reynolds number simulations is a distinctive upward fluid jet, shown in figure 1.3a, that was caused by the contraction of the porous layer. This contraction was representative of two neighbouring cilia moving towards one

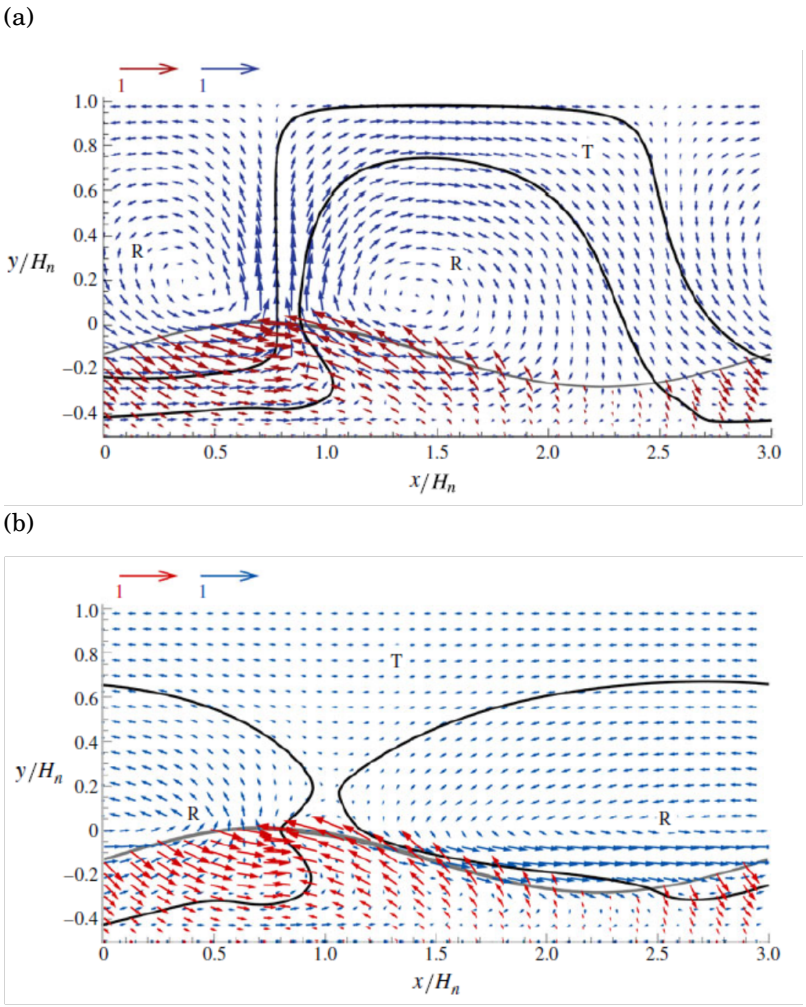

Figure 1.3: Simulation results for (a) Re = 1 showing the formation of two rotating cells and (b) Re = 2000 showing the formation of a single rotating cell. Red arrows indicate velocity of the solid phase, blue arrows indicate the velocity of the liquid phase. Graphic reproduced with permission from Hussong et al. (2008) [22].

another as a result of the phase difference between their beating cycles [22]. In the viscosity dominated regime, the fluid on the left side of the jet (as it is seen in figure 1.3a) was drawn down and back into the porous layer by the increasing porosity caused by its expansion [22]. This formed a recirculating cell that was not mirrored on the opposite side of the jet, so that fluid on the right side of the jet was drawn down and into the recirculating cell of the neighbouring jet. This asymmetry caused a net flow in the direction of the metachronal wave (to the right) along a transitory channel that was "driven" by a series of recirculating cells [22].

In the inertia dominated regime, they observed a similar yet distinct behaviour. In the results shown in figure 1.3b, there was a significantly smaller upward jet of fluid that flowed almost entirely to the left and back down into the porous layer forming a single rotating cell (per

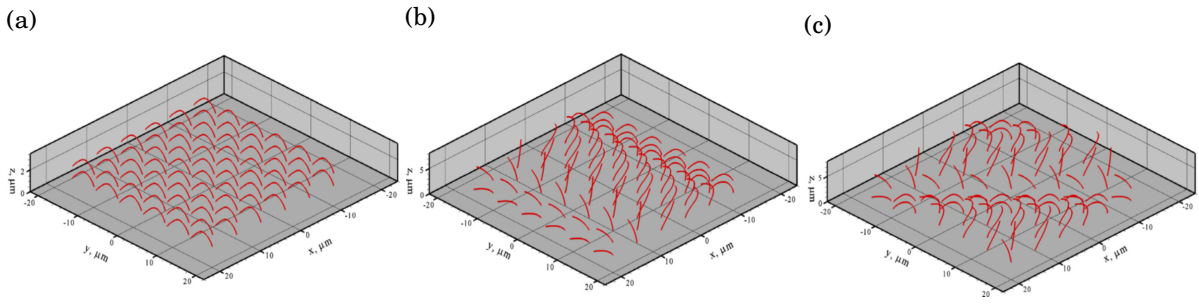

Figure 1.4: Graphical representations of three different cases of cilia phase: (a) Synchrony (b) Antiplectic metachrony (c) Antiplectic and diaplectic metachrony. Graphic reproduced with permission from Jayathilake et al. (2012) [24].

metachronal wavelength). The rotation of this single cell caused a very slow net flow of fluid along its top surface, in the opposite direction to the metachronal wave [22]. These results indicated that metachrony plays a major role in the process of muco-ciliary clearance, by showing that it alone is enough to induce a directional flow in a viscous fluid.

Jayathilake et al. [24] have investigated the effect of both antiplectic and diaplectic metachrony, just as it was observed in pulmonary cilia by Gheber and Priel [15]. Jayathilake et al. used a three dimensional cilia model to evaluate fluid flow in both the stream-wise and span-wise directions. For simplicity, we refer to the direction of the active stroke as the x direction, and the orthogonal in the plane of the epithelium as the y direction. The key factor of these simulations is that they included the full three dimensional cilia beat profile, so that the work done by the recovery stroke in the y direction can be taken into account. It should also be noted that these simulations included only the PCL with no mucus layer. This model was used to investigate the effectiveness of an array of 72 cilia in three different cases [24], as shown in figure 1.4:

A. No phase difference between cilia (synchrony)

B. Phase difference in the negative x direction (antiplectic metachrony)

C. Phase difference in both the negative x direction and the positive y direction (antiplectic and diaplectic metachrony)

The results of these simulations showed that in case A there was a large fluctuation in the direction of fluid flow over time, but there was still a net flux of fluid in the positive x direction, as can be seen in figure 1.5a. This indicated that the asymmetry of the cilia beat profile was only partly effective in causing directional fluid flow [24]. Fluctuations in flow direction were also present in the y direction. In case B the introduction of a phase step to create the metachronal wave dramatically reduced the fluctuation in fluid velocity in both the x and y directions. This resulted in a significant increase of net flux in the positive x direction and a reduction of the net flux in the negative y direction. Case C showed a small additional increase of net flux in

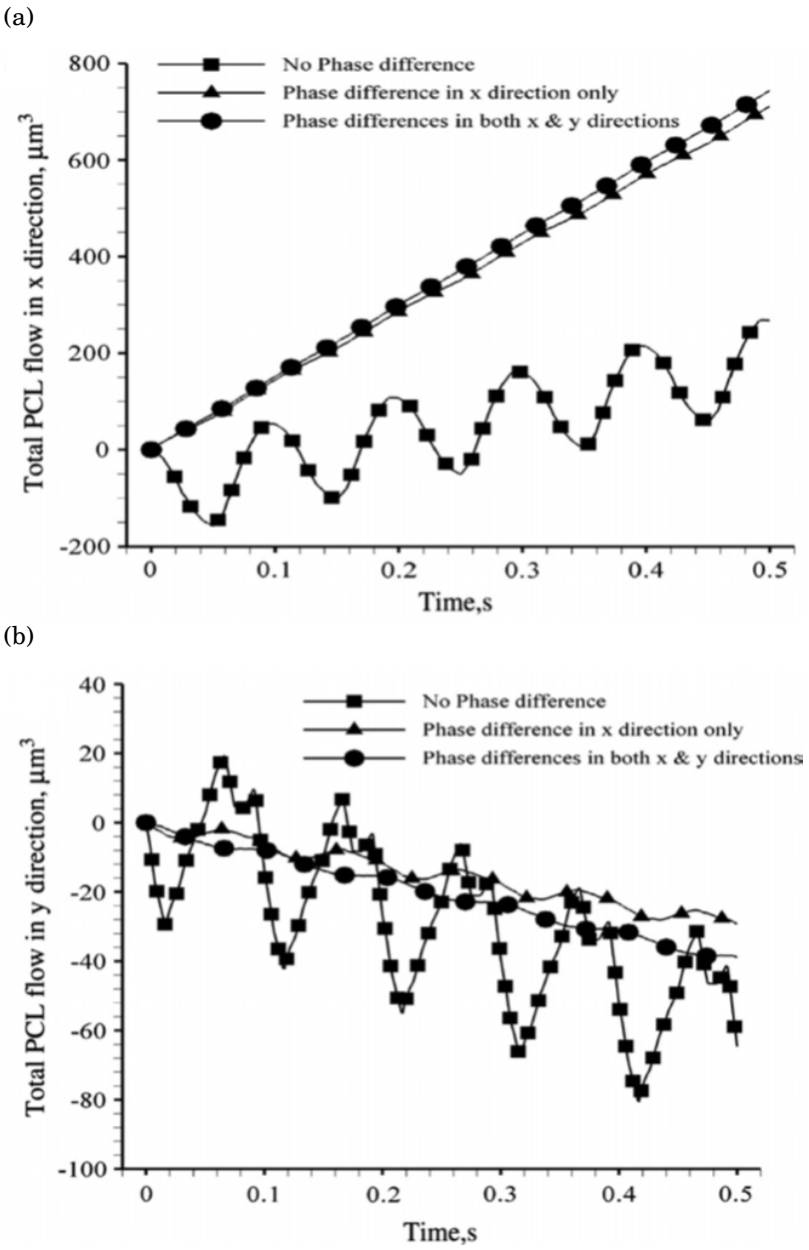

Figure 1.5: Fluid flow over time in (a) the x direction and (b) the y direction for three different cases of metachronal coordination. Graphic reproduced with permission from Jayathilake et al. (2012) [24].

the positive x direction, as well as a small increase of net flux in the negative y direction when compared to the results from case B. The resulting velocity in the y direction is roughly 5% of that in the x direction. Further simulations of case C [24] showed that there was a linear increase in x velocity with increasing cilia beat frequency, in agreement with other 2D and 3D simulation results [7, 22, 41]. We have investigated this behaviour further using our own numerical model in section 5.1.

Ding et al. [11] used a regularised Stokeslet method with the cilia beat pattern defined by Fulford and Blake [14] to investigate the effectiveness of both fluid flow and mixing driven by cilia beating. They compared results for the synchronised case, symplectic metachrony and antiplectic metachrony. Their results showed that both types of metachrony improved fluid flow compared to the synchronised case, although they noted that there are specific cases where a symplectic metachronal wave with a long wavelength could generate fluid flow that is slower than in the synchronised case [11]. They observed that the optimal case for both fluid flow and mixing occurred when the cilia were beating in an antiplectic wave with a phase step between cilia of $\Delta\phi = \pi/2$. They also observed that optimal fluid transport universally corresponded with optimal mixing, and that there was minimal difference between antiplectic and symplectic metachrony in their results.

Chateau et al. [6] conducted a similar investigation to determine how volumetric flow and fluid mixing were affected by the metachronal wavelength of a cilia array. Their model was based on the Immersed boundary Lattice Boltzmann method described by Li et al. [32]. This model was used to simulate cilia driven fluid flow in a binary fluid with two distinct layers of Newtonian fluid with different viscosities. They looked into the development of metachronal waves within the cilia array by allowing the beating cilia to change their movement speed in reaction to the forces experienced from the fluid around them. They found that the cilia were able to coordinate from an initially random state into a metachronal wave purely by the hydrodynamic forces between them. This behaviour could be controlled by tuning the strength of the forces that were felt by each cilium [6]. They observed that the forces between the fluid and the cilia during the active stroke of each cilium were much higher in the case of antiplectic metachrony, suggesting that more energy was being transferred from the cilia to the fluid in this case. This also meant that in their simulations the active stroke was slower than the recovery stroke for an antiplectic wave which is different from in vitro observations [14].

Chateau et al. [6] also considered the effects of metachronal wavelength on fluid flow and mixing. To observe this, they imposed a metachronal wave on the cilia array by introducing a fixed phase step ($\Delta\phi$) between adjacent cilia, and removing the feedback force experienced by the cilia. Their results, shown in figure 1.6, indicated that antiplectic waves ($\Delta\phi > 0$) were more effective in driving fluid flow, in agreement with Ding et al [11]. They also observed that the improvement of fluid flow due to metachrony was reduced when the cilia spacing was larger which they attribute to the cilia having less influence on each other when there was more fluid between them [6]. They reasoned that the improved performance of an antiplectic wave was due to the clustering of cilia during the recovery stroke, causing a greater net energy transfer in the direction of the active stroke, and that the opposite was true in the case of a symplectic wave.

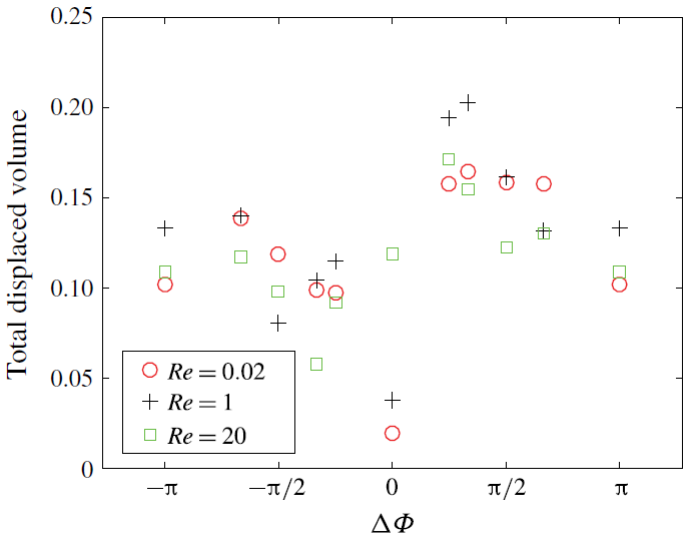

Figure 1.6: Results showing that the total displaced volume of fluid is dependent on the phase step between the beat cycles of adjacent cilia. Graphic reproduced with permission from Chateau et al. (2017) [6].

1.2 Mucus Layer Formation

1.2.1 Transition between PCL and Mucus

It is apparent from experimental results that the separation of PCL and mucus plays a crucial role in muco-ciliary clearance (MCC) [41, 46], allowing the cilia to move freely within the PCL unhindered by visco-elastic effects, while the viscous mucus captures inhaled particles and bacteria to transport them out of the lungs [46].

The clear boundary between the two layers is generally taken as a given when modelling MCC, although Chatelin and Poncet [7] considered the effects of a continuous boundary on the efficiency of MCC. The fluid was treated as a single fluid layer with a continuous relationship between viscosity and depth. Two different viscosity profiles were considered: a sigmoid profile, and a linear profile. Parametric dependencies were investigated in each case [7]. In these simulations the efficiency of MCC was represented by the scalar quantity U that represents the net flow of fluid in the x direction at the top of the fluid region. The cilia beat profile used in these simulations was the same as in Li et al. [32], described earlier.

The length of cilia used in the model was varied between 3μm and 12μm, with a constant fluid height of 13μm. The "transition length" of the sigmoid profile was seen as the position of the boundary between PCL and mucus, and this was kept constant at 8μm [7]. Results from these simulations showed that fluid flow rate increased with cilia length and peaked when the cilia length was slightly larger than the transition length. This is in agreement with similar studies that have shown that MCC is most efficient when only the active stroke of the cilium beat

penetrates the mucus layer (ML) [41, 44].

In further simulations the ratio between the viscosity of the mucus and the PCL (β) was varied over a large range showing that there was a distinct peak in fluid flow rate for the sigmoid profile that was not present for the linear profile. In both cases there was a significant decrease in fluid flow rate at very high mucus viscosity, which could be representative of the low level of MCC present in Cystic fibrosis patients [7, 12]. Other simulations that allow for variation of beat frequency have shown that in situations such as this, where the PCL has a higher viscosity, the cilia beating frequency decreases and the resulting rate of MCC is significantly slower [45].

The final set of simulations presented by Chatelin and Poncet [7] investigated the relationships between the three major parameters of the sigmoid viscosity profile, namely: the Viscosity ratio between mucus and PCL (β), the viscosity transition stiffness (γ), and the transition length (δ). The relationship between β and γ displayed in figure 1.7a shows that the most efficient MCC occured for a moderate β value and a large γ value [7], indicating that mucus viscosity could improve MCC, if the boundary between PCL and mucus were sharp enough to minimise the effect of the recovery stroke on the mucus layer. The relationship between β and δ shown in figure 1.7b supported this idea further by showing that the most efficient MCC occured with similar values of β and values of δ around the cilium length ($6-9\mu$m). Which also indicated that was most effective when the cilia only interacted with the mucus layer during their active stroke. The relationship between γ and δ shown in figure 1.7c indicated again that a sharp boundary between the two layers makes for efficient MCC, and that this boundary being at around the same level as the cilium length also improved MCC efficiency [7].

1.2.2 Peri-ciliary Brush

Recent experimental research has shown that the physical structure of pulmonary cilia is more complex than in the models that we have discussed so far [5, 26]. A matrix of tethered polymer strings have been observed attached to the cilia, forming what is called a "Peri-ciliary Brush" (PCB) [5]. The presence of the PCB has two major implications: firstly the tendency for the PCB to be more dense closer to the base of the cilia could mean that it plays a role in expelling mucins and other particles from the PCL, creating the two distinct layers (PCL and mucus layer) and maintaining ciliary mobility. Earlier work on the separation of the two layers speculated that it could be caused by either thixotropic forces from the beating cilia liquefying any mucus that is present between the cilia, or capillarity emerging from the dense packing of cilia suspending the PCL between the cilia to prevent mixing of the two layers [50]. The mechanics of mucin conformation and the separation of the two fluid layers are explored further in section 1.2.3. The second implication is that the tethered polymer chains could cause elastic forces between neighbouring cilia and contribute to the emergence and maintenance of a metachronal wave [26].

The gel-on-brush model proposed by Button et al. [5] suggested that the PCB prevents mucins and inhaled pathogens from entering the PCL, as well as forming a supportive structure that

(a)

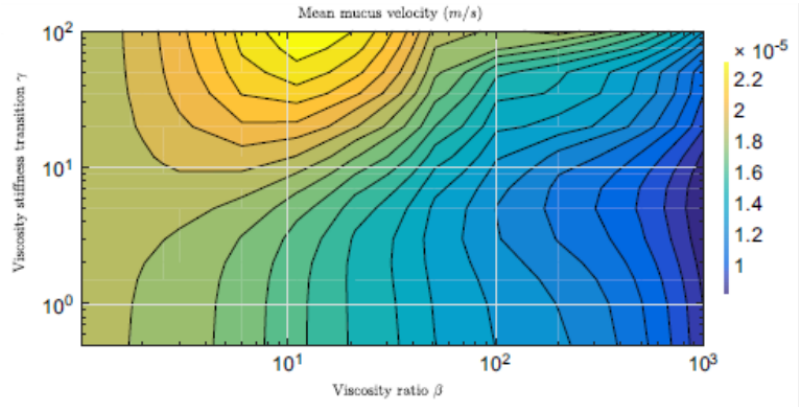

(b)

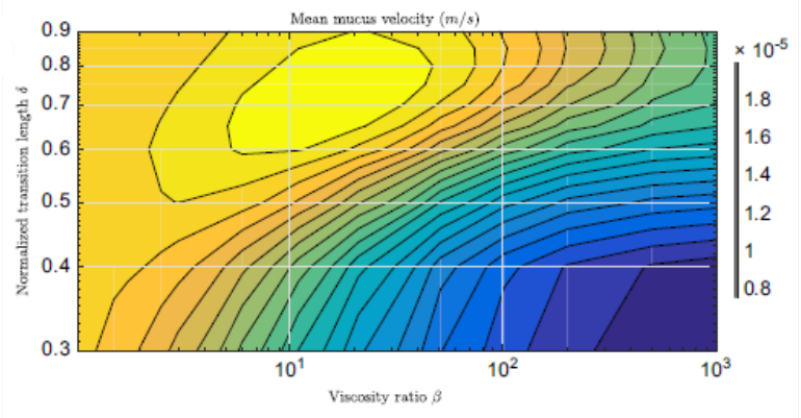

(c)

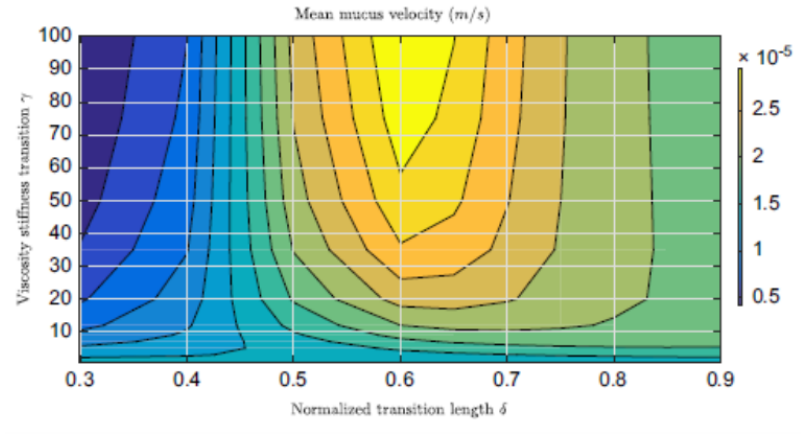

Figure 1.7: Relationships between the key parameters of the mucus/PCL binary fluid system with respect to mucus velocity. (a) mucus/PCL viscosity ratio (β) and viscosity stiffness transition γ (b) β and transition length δ (c) δ and γ. Graphic reproduced with permission from Chatelin and Poncet (2016) [7].

prevents the PCL from being compressed due to an "osmotically active mucus layer" [5]. Evidence for the existence of a PCB has been presented as electron microscope images of rapidly frozen human bronchial epithelial samples that showed a dense mesh of polymer chains between cilia. These mucins could not be removed by vigorous washings [5] that served to strip mucus from the samples, so it was concluded that these mucins were tethered to the cilia membranes.

The mesh size was quantified by introducing two sizes of dextran molecules (40nm diameter, and 2nm diameter), and measuring the penetration depths of the two molecules types [5]. These molecules were labelled with different florescent colours (green and red respectively). Following this experiment, a wider range of sizes were introduced and the resulting colour gradient of the sample was used to generate an exclusion profile for the PCL. The resulting exclusion profile was consistent with the proposition that the mesh density increases towards the base of the cilia.

The work of Button et al [5] went on to show that the presence of the tethered polymer mesh in the PCL served to fix its minimal osmotic modulus. This means that if the hydration of the airway increased, the ML becomes more hydrated and the PCL remains largely unaffected. The same can be said of dehydration, with the limit that when the osmotic modulus of the ML becomes greater than that of the PCL, the PCL will start to become dehydrated and compressed [5]. This compression would severely impede ciliary motion; reducing and eventually stopping muco-ciliary clearance. This behaviour can be linked to the symptoms of both cystic fibrosis (CF), and chronic obstructive pulmonary disease (COPD) which are discussed in Section 1.3.

Further investigation into the composition of the PCB was carried out by Kesimer et al. [26]. In this work the distribution of mucins was determined by karatan sulphate (KS) staining; initially showing that there was a large difference between the spatial distribution of KS and mucins 5AC and 5B. More specifically these two mucins were mainly present in the mucus layer, while there was intense KS staining in the PCL [26]. These results suggested that there were different mucins present within the PCL that were attached to the cilia. Subsequent experiments used staining by immuno-fluorescence to identify that MUC1 was present at the base of the cilia attached to the microvilli, and MUC4 was present along the ciliary shafts. These mucins were also found in the mucus layer within "ciliary plumes" [26], after apparently being shed from the cilia membrane. These results gave a more detailed account of exactly what the PCB is, as well as re-enforcing the idea that the mesh became more dense towards the base of the cilia by showing that there were also mucins attached to the microvilli between cilia.

1.2.3 Mucin Hydration

The mucins that form the mucus layer originate from goblet cells within the epithelium and submucosal glands [47]. The mucins are released within the goblet cells and glands as condensed grains made up of cross-linked polymer chains. These polymers hydrate during the process of exocytosis to form a spheroid of entangled polymer gel up to 20μm in diameter within 4-8 seconds [47]. The rapid expansion of mucins is driven mainly by a Donnan potential between the ions

distributed within the polymer gel and the free ions in the surrounding fluid [43]. Expansion is initially prevented by the presence of Ca^{2+} ions acting as cross-linkers within the polymer grain; during exocytosis these ions are removed by reacting with HCO_3^- and replaced with Na^+ from the PCL as the polymer hydrates. Thus the crosslinks are removed and the gel is free to expand. The hydration of mucins has been observed to closely follow the first order kinetics of swelling gels [47] as derived by Keener et al. [25]

$$r(t) = r_f - (r_f - r_i)e^{-t/\tau_s} \tag{1.1}$$

where τ_s is the characteristic time of swelling, and r_i and r_f denote the initial and final radius of the gel respectively. It has also been shown by Keener et al. [25] that there is a linear relationship between τ_s and r_f^2 for polymer gels, allowing the diffusion coefficient of the gel to be determined as $D = r_f^2/\tau_s$.

Electron micrograph images from the work of Verdugo [47] showed two stages of mucin secretion in vitro: the appearance of convex bulges as mucins begin to emerge from the pores of goblet cells, and the presence of mucins as discrete spherical globules once exocytosis was complete.

The presence of goblet cells in the epithelium means that there are gaps of 10μm diameter between ciliated areas [2]. The effect that these gaps have on MCC remains to be seen, although results from Yang et al [51] showed that an increase in cilia spacing could reduce the net fluid flow caused by each cilium beat. This also means that after exocytosis, the mucin emerges into an unciliated area creating a region within the pulmonary system where the mucus layer can effectively reach from the epithelium to the mucus-air interface. The effect that this has on MCC also remains to be seen.

1.3 Disease States

There are three major diseases that can affect MCC: Cystic Fibrosis (CF), Asthma, and Chronic Obstructive Pulmonary Disease (COPD). In this section each of these diseases is discussed, and the symptoms of each that are relevant to MCC are identified.

1.3.1 Cystic Fibrosis

Cystic fibrosis (CF), also known as mucoviscidosis, is characterised by “the build-up of thick, sticky mucus in multiple mucin-producing organs, such as the lungs, sinuses, intestine, pancreas and reproductive organs.” [12]. As discussed in section 1.1.1, an increase in mucus viscosity can directly affect MCC. Experimental data from Gustafsson et al. [17] suggested that the high viscosity of CF mucus was due to the incomplete expansion of mucins. CF can also lead to dehydration of epithelial surfaces, that would cause a decrease of overall fluid depth and lead to

further reduction of ciliary beating as discussed in section 1.2.2. A reduction of PCL thickness due to dehydration can also allow mucus to adhere to the epithelial surface, stopping MCC entirely [12].

Situations where MCC stops, known as mucus stasis, can start a cycle of infection and immune system response that can be fatal [12]. In brief: mucus stasis encourages bacterial growth within the lungs, and as a response to this, neutrophils are released from the epithelium. The neutrophils become trapped in the viscous mucus and release their DNA upon death, increasing the viscosity of the surrounding mucus and causing further mucus stasis.

1.3.2 Asthma

The symptoms of asthma, although similar in many ways to those of CF and COPD, are identified to have different root causes. Large collections of viscous mucus can plug the airways in cases of severe asthma [37] with evidence showing that this can be attributed to a combination of mucin hyper-secretion and goblet cell hyperplasia [42]. This results in a scenario where the reduced number of ciliated cells (replaced by goblet cells) are insufficient to clear the large amounts of mucus being produced [37].

Experimental results have also indicated the presence of several other components in the mucus of asthma patients that were rarely present in control samples. The presence of MUC2 alongside an increase in MUC5B indicated a change in the function of goblet cells which would lead to the mucus in asthma patients having different rheological properties [37]. Experimental results have indicated that plasma proteins, and even DNA, were present in the mucus of some asthma patients [38]. The source of these proteins is thought to be post-capillary venules close to the epithelium. This too would cause a change in the rheology of the mucus, and possibly impede proper mucin hydration due to the dilution of PCL with plasma.

Mucin tethering, which is also present in CF patients, is a significant contributor to the development of mucus plugs in asthma patients [42]. Recent experimental work has shown that MUC5AC has a tenancy to tether to the epithelial surface in asthma patients [4]. The cause of the tethering is unknown at this time.

1.3.3 COPD

Chronic obstructive pulmonary disease (COPD) is technically not a disease in its self, but the term for airflow obstruction associated with chronic bronchitis and emphysema [1]. Common symptoms shared by COPD and Asthma are goblet cell hyperplasia, and submucosal gland enlargement [37]. However, the submucosal glands in COPD patients have been observed to have an increased number of mucous cells and a corresponding decreased number of serous cells resulting in hyper-secretion of MUC5B specifically.

Another important factor of COPD is "squamous metaplasia" of the epithelial cells [1], meaning that both goblet cells and ciliated cells become flattened and unable to function. This

causes there to be large areas of the epithelium where no cilia are present, which has a drastic effect on MCC and could allow an excess of mucus to build up in the lungs.

1.4 Summary

The wide range of existing work in the field of cilia driven fluid flow has provided us with an insight into the important factors that must be considered while studying the mechanics of cilia beating.

The internal structure of a cilium has been well documented, which gives us a strong basis for modelling a cilium and it's distinctive beating profile. Simulation results from several different sources have demonstrated the importance of metachrony in cilia driven flow, and shown that even small changes to the metachronal wavelength and cilium spacing can affect fluid flow.

Investigations into the rheology of the fluid surrounding the cilia have shown that the separation of mucus and PCL into two distinct layers is vital for effective cilia driven flow. They have also shown that the differences in rheology between the two layers plays a role in generating fluid flow. Multiple sources have shown that the cilia only penetrate into the mucus layer during the active stroke, which increases the flow rate of mucus.

Previous work looking at the process of mucin hydration has helped us to understand the visco-elastic properties of the mucus layer and how it is formed. This work has also given us some information about the cells that make up the epithelium, and that not all of them are ciliated.

Studies of the diseases that can affect the pulmonary epithelium have given us some idea of the limitations of cilia driven flow, and how changes to the rheology of the mucus and the structure of the epithelium can cause cilia driven flow to stop completely.

The work included in this chapter has given us a strong foundation on which to build a representative numerical model of the system, and used that model to take a more in-depth look at some of the phenomena that have been observed previously.

2

COMPUTATIONAL METHODS

In this chapter we give details of the methods that we have used in our work to model cilia driven fluid flow. We describe the equations that form the basis of the lattice Boltzmann algorithm and how these equations describe fluid flow, along with the results from benchmarking tests that we carried out by simulating the well documented behaviour of fluid flowing past a stationary cylinder. We also describe how we have represented a beating cilium as an immersed boundary that interacts with the fluid lattice through external forces.

We provide details of how our computational model has been adapted to simulate the behaviour of a binary fluid with visco-elastic properties, and results from benchmarking tests to ensure that visco-elastic behaviour is properly represented in our model. We give a clear outline of how fluid flow rate is derived from our simulation results and define the boundary conditions and simulation parameters that are used in all of our simulations of cilia driven fluid flow. We present the results of a convergence test that we conducted to select a numerical Reynolds number that would give us results that are representative of the in vivo system without making the run times of our simulations excessively long.

We give an outline of the program that we have written to carry out our simulations complete with pseudo-code of the functions used for each step of the lattice Boltzmann algorithm, with some details of how our code has been optimised for running on a GPU.

2.1 Building the Numerical Model

2.1.1 The Immersed Boundary Lattice Boltzmann Algorithm

The lattice Boltzmann method is based on the idea that a fluid can be discretised as an array of static Eulerian nodes, each of these nodes is assigned a set of lattice vectors $\vec{c}_i$ that point in the directions of the adjacent nodes [28]. Each lattice vector also has a population density component $f_i(\vec{x},t)$ associated with it, and the magnitude of each component represents a fraction of the population density of the fluid at that node. In two dimensions it is standard practice to assign nine vectors to each node as shown in Fig. 2.1, forming a D2Q9 lattice. The evolution of

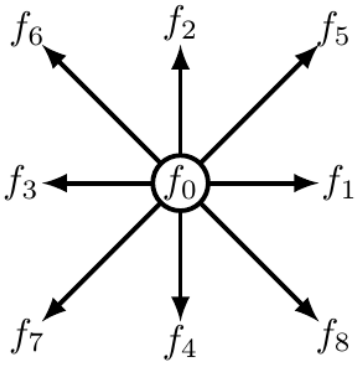

Figure 2.1: A representation of the population densities assigned to each node in a D2Q9 lattice Boltzmann fluid node.

population densities at each time step is governed by the lattice Boltzmann evolution equation:

$$f_i(\vec{x}+\vec{c}_i, t+1) - f_i(\vec{x}, t) = \Omega_i(\vec{x}, t). \tag{2.1}$$

This means that for each time step the population density associated with a lattice vector is passed to an adjacent node in the direction of that vector (streaming). The passage of population density from one node to another is modified by some collision operator $\Omega_i(\vec{x}, t)$ [48]. We initially used the BGK collision operator [28] given by

$$\Omega_i = -\frac{1}{\tau}\left[f_i - f_i^{(0)}\right] \tag{2.2}$$

where τ is the relaxation time of the fluid and $f_i^{(0)}$ represents the equilibrium particle distribution calculated from the fluid density $\rho(\vec{x}, t)$ and velocity $\vec{u}(\vec{x}, t)$ at each node by

$$f_i^{(0)} = \rho w_i \left[1 + \frac{\vec{c}_i \cdot \vec{u}}{c_s^2} + \frac{(\vec{c}_i \cdot \vec{u})^2}{2c_s^4} - \frac{\vec{u}^2}{2c_s^2}\right]. \tag{2.3}$$

with w_i representing weight functions that are defined as part of the dimensions of the lattice, and c_s representing the dimensionless speed of sound on the lattice $c_s = \frac{1}{\sqrt{3}}$. The inclusion of immersed boundaries requires a external force term $F_i(\vec{x}, t)$ to be added to equation 2.1, meaning that the modified evolution equation becomes

$$f_i^{(1)} = \left(1 - \frac{1}{\tau}\right) f_i + \frac{1}{\tau} f_i^{(0)} + F_i \tag{2.4}$$

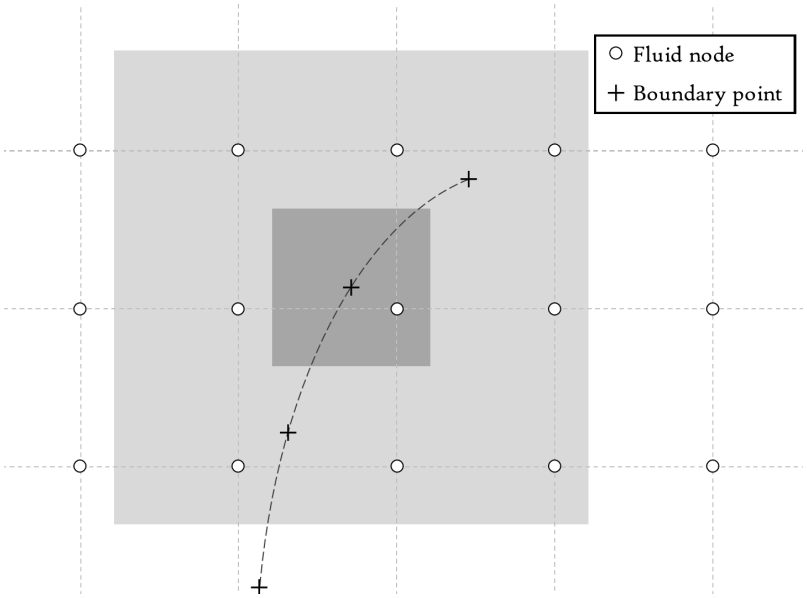

Figure 2.2: A set of Lagrangian points representing an immersed boundary super imposed on a grid of Eulerian fluid nodes, including the support domain of a single boundary point.

where $f_i^{(1)} = f_i(\vec{x} + \vec{c_i}, t+1)$. Equation 2.4 represents the backbone of our numerical model, controlling the streaming of fluid between nodes as well as the interactions between fluid and boundaries [32]. The macroscopic quantities of density and velocity are calculated at each time step from f_i by

$$\rho(\vec{x}, t) = \sum_i f_i(\vec{x}, t) \tag{2.5}$$

$$\rho(\vec{x}, t)\vec{u}(\vec{x}, t) = \sum_i \vec{c_i} f_i(\vec{x}, t) + \frac{1}{2}\vec{F} \tag{2.6}$$

where $\vec{F}$ is the macroscopic value of the external force at each node. These values are used to define the equilibrium conditions for the next time step as in equation 2.3. In our model the relaxation time τ is intrinsically linked to the Reynolds number of the system such that

$$Re = \frac{UN}{c_s^2(\tau - 1/2)} \tag{2.7}$$

where U is a characteristic speed in lattice units per time step which in this case is the average speed of a cilium tip, and N is the characteristic length in lattice units which is the length of a cilium [28].

We determine the external force acting on the fluid by first defining a series of Lagrangian points which are representative of the boundary geometry, as demonstrated in Fig. 2.2 [32]. We

calculate the interaction forces between the boundary points and fluid nodes by interpolating equation 2.6, resulting in the equation

$$\vec{F}_s = \sum_{j \in D_s} 2\rho_j \tilde{\delta}(\vec{x}_j - \vec{x}_s)(\vec{u}_s - \vec{u}_j) \tag{2.8}$$

which determines the force of the fluid acting on a single boundary point F_s based on the difference between the boundary velocity u_s and the fluid velocity u_j at nodes within the support domain of the boundary point D_s [36]. The contribution from each node is scaled by a smoothed delta function $\tilde{\delta}(\vec{x}_j - \vec{x}_s)$ which takes the form

$$\tilde{\delta}(\vec{x}_j - \vec{x}_s) = \tilde{\delta}_x(|x_j - x_s|)\tilde{\delta}_y(|y_j - y_s|) \tag{2.9}$$

with:

$$\tilde{\delta}_{x,y}(r) = \begin{cases} \frac{1}{3}\left(1 + \sqrt{-3r^2 + 1}\right) & \text{for } 0 \le r \le 0.5 \\ \frac{1}{6}\left[5 - 3r - \sqrt{-3(1-r)^2 + 1}\right] & \text{for } 0.5 < r \le 1.5 \\ 0 & \text{otherwise.} \end{cases} \tag{2.10}$$

The delta function also defines the support domain of each surface point as a square of side 3 lattice units centred at that point, as shown in figure 2.2 [32]. The force at the surface points is then spread to the surrounding fluid nodes by

$$\vec{F}(\vec{x}_j, t) = \sum_{s \in D_j} \vec{F}_s \tilde{\delta}(\vec{x}_j - \vec{x}_s)\Delta s \tag{2.11}$$

which calculates the external force at point j as the sum of the forces from all boundary points within the support domain D_j [36], scaled by the same delta function as described in equation 2.9, and the boundary point separation Δs. We use the macroscopic external force $\vec{F}$ to modify the velocity of the affected fluid nodes through equation 2.6. We also represent the external force in terms of lattice vector components using

$$F_i = \left(1 - \frac{\Delta t}{2}\right) w_i \left[\frac{\vec{c}_i - \vec{u}}{{c_s}^2} + \frac{\vec{c}_i \cdot \vec{u}}{{c_s}^4}\vec{c}_i\right] \cdot \vec{F}. \tag{2.12}$$

We use these component forces in equation 2.1 to modify the collision operator to include the external force associated with the immersed boundary. We note that all of the above equations are written in lattice units so that the lattice spacing (Δx) and the time step size (Δt) are equal to unity. We set the lattice spacing so that the length of a cilium is 32 lattice units (LU), so for a $6\mu m$ cilium the lattice spacing is $\Delta x = 187.5$nm. We vary the time step size depending on the Reynolds

number to maintain an optimal relaxation time and to keep the fluid velocity significantly lower than the speed of sound on the lattice [28]. Unless otherwise stated we set the Reynolds number to be equal to unity, meaning that the scaled time step size is also fixed such that $\Delta t = 66.7$ns.

Due to the low Reynolds number of the system that we are modelling ($Re \leq 1$), we have used the two relaxation time (TRT) method to avoid significant inaccuracies in our simulations [28]. In the case of the BGK collision operator the truncation error in the model increases proportionally with the relaxation time (τ) [28], and to increase the viscosity of our fluid we must increase τ. The TRT method allows us to alter the viscosity of our fluid without directly affecting the accuracy of our simulations through the use of a second relaxation time. In this case the truncation error of a simulation is related to a different parameter Λ which is defined as

$$\Lambda = \left(\tau^{+} - \frac{1}{2}\right)\left(\tau^{-} - \frac{1}{2}\right) \tag{2.13}$$

where τ^{+} dictates the viscosity of our fluid in the same way as τ for the BGK collision operator, and τ^{-} is a free parameter. By fixing Λ we ensure that the truncation error of our simulations does not increase when we increase viscosity. We use a value of $\Lambda = 1/6$ to optimise our simulations for pure diffusion problems [28]. The standard implementation of the TRT method is based on the fact that for each velocity component $\vec{c}_i$ there is an opposing component where $\vec{c}_{\bar{i}} = -\vec{c}_i$ [28]. This is used to generate symmetric and antisymmetric parts of the population by

$$f_i^{+} = \frac{f_i + f_{\bar{i}}}{2} \quad f_i^{-} = \frac{f_i - f_{\bar{i}}}{2}. \tag{2.14}$$

Similarly for the equilibrium population

$$f_i^{(0)+} = \frac{f_i^{(0)} + f_{\bar{i}}^{(0)}}{2} \quad f_i^{(0)-} = \frac{f_i^{(0)} - f_{\bar{i}}^{(0)}}{2}. \tag{2.15}$$

The symmetric and antisymmetric populations are used in an alternative collision operator to the BGK method shown in equation 2.2 where

$$\Omega_i^{TRT} = -\frac{1}{\tau^{+}}\left(f_i^{+} - f_i^{(0)+}\right) - \frac{1}{\tau^{-}}\left(f_i^{-} - f_i^{(0)-}\right). \tag{2.16}$$

We used the TRT method to ensure that when at low Reynolds numbers ($Re < 1$) the increase in viscosity did not alter the accuracy of our results.

In our 3D model we used the same lattice Boltzmann algorithm as described above with a 3D array of fluid nodes that each have 15 components (D3Q15) as shown in figure 2.3.

We used the Immersed boundary method in our model to represent each cilium as a set of boundary points that are separated by a single lattice unit . The dimensions of the simulated

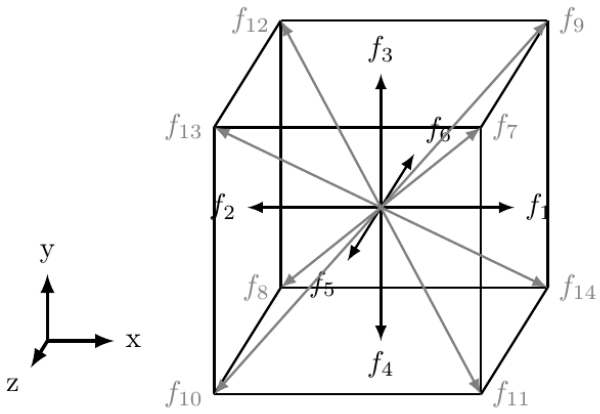

Figure 2.3: A representation of the population densities assigned to each node in a D3Q15 lattice Boltzmann model.

fluid region were always defined relative to the cilium length and the cilium spacing such that the x dimension was given by the cilium spacing multiplied by the number of cilia and the height of the fluid region was double the cilium length.

Our model was written in CUDA so that we could perform simulations in parallel on a GPU. The immersed boundary lattice Boltzmann (IBLB) algorithm is well suited to parallel programming due to the calculations for each time step being completely localized [28].

2.1.2 Benchmarking: Flow past a cylinder

The characteristics of fluid flowing past a stationary cylinder are well documented for a range of parameters, and this system is known to be very sensitive to the accuracy of the model used to simulate it [32, 36]. The key parameter in these simulations is the Reynolds number (Re) which represents the ratio of inertial and viscous forces present in the system. For these simulations we calculated the Reynolds number by [32]

$$Re = \frac{|\vec{U}_0|D}{{c_s}^2\left(\tau - \frac{1}{2}\right)} \tag{2.17}$$

Where $\vec{U}_0$ is the inlet velocity of the fluid, D is the diameter of the cylinder, and the denominator is the equation for shear viscosity (ν) as defined by the lattice Boltzmann parameters [48]. In a situation where $Re = 30$ the flow past a cylinder is known to form a steady closed wake with two recirculating cells.

The parameters of this closed wake are very sensitive to the model accuracy, specifically the positions of the vortex cores and the length of the wake [32, 36]. Graphical representations of these parameters are shown in figure 2.4.

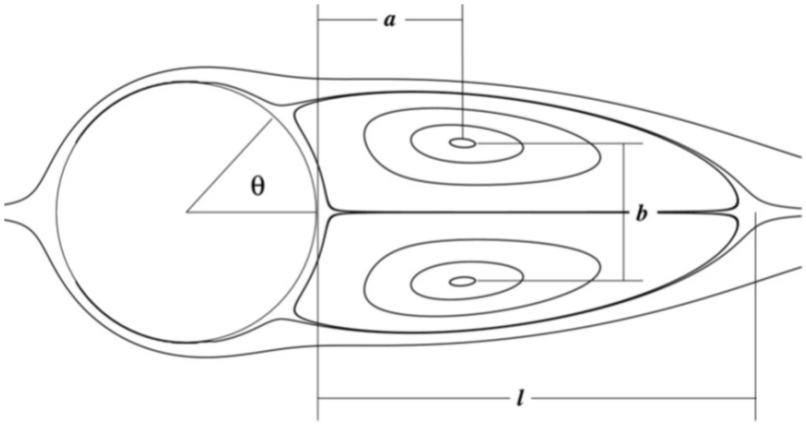

Figure 2.4: Streamline diagram of the flow past a cylinder with $Re = 30$, including wake parameter definitions. Graphic reproduced with permission from Pinelli et al. (2010) [36].

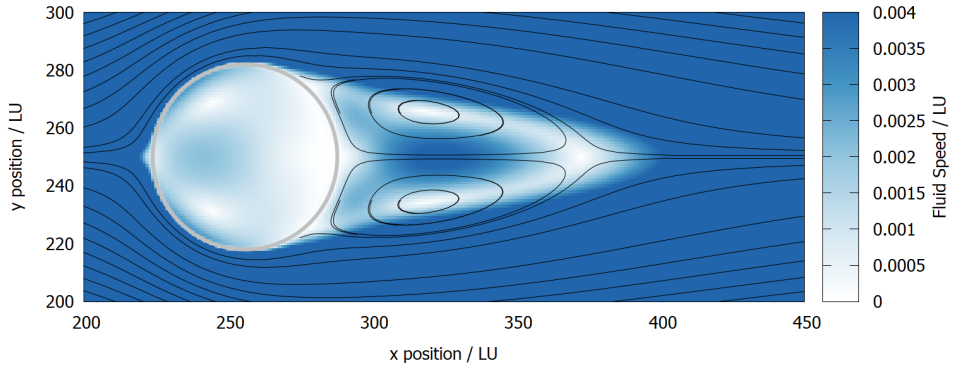

Figure 2.5: Streamline diagram of the flow past a cylinder with $Re = 30$ showing a closed wake with 2 rotating cells

We have run simulations with our IBLB model using a Zou He velocity boundary to set the inlet velocity $\vec{U}_0 = (0.125, 0)$ [52] and non-slip boundary conditions on the top and bottom boundaries of the fluid region [48]. Results from these simulations showed the same closed wake behaviour with two rotating cells as shown in Fig. 2.5. The diameter of the cylinder in these simulations was 32 lattice units. Note that the fluid region for this simulation was 1000x500 nodes, and the area shown is only a small fraction of this.

The wake parameters from our simulations are compared with the results from the literature [10, 32, 36] in table 2.1, as well as experimental results from [10] to verify the accuracy of our model. Its is clear from this comparison that our simulation results demonstrated the same behaviour as the results from the literature.

Another well understood behaviour of fluid flow past a cylinder is the emergence of a Von Karman vortex street at larger Reynolds numbers. This is characterised by a series of vortices being shed from the wake of the cylinder. By setting $Re = 150$ we were also able to simulate a Von Karman vortex street as shown in Fig. 2.6.

Table 2.1: Cylinder closed wake parameters

Source	a/D	b/D	l/D
Our Simulations	0.56	0.56	1.72
Li et al. [32]	0.59	0.55	-
Pinelli et al. [36]	0.56	0.52	1.70
Coutanceau et al. [10]	0.54	0.54	1.55

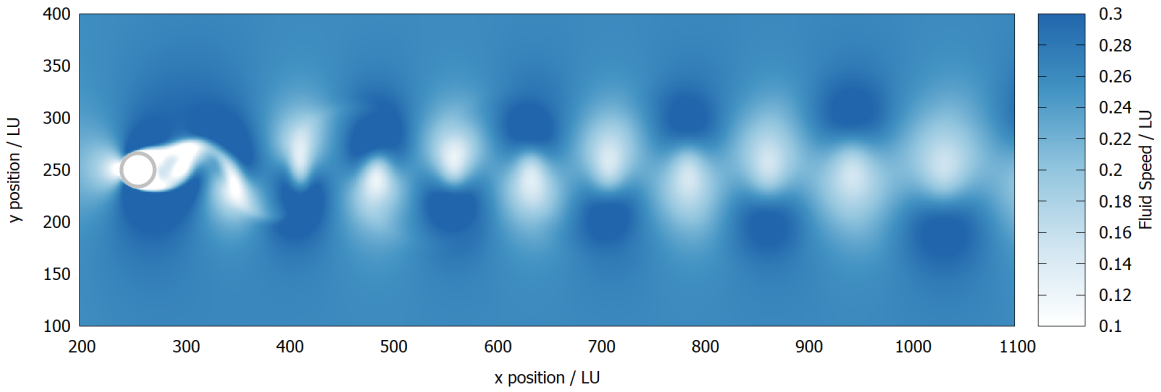

Figure 2.6: Example of a Von Karman vortex street forming in the wake of a cylinder with $Re = 150$.

2.2 Modelling the Cilium as an Immersed Boundary

Each cilium in our simulations was represented by a filament of boundary points that moved in a prescribed pattern. The position of each boundary point was calculated for every time step using a truncated Fourier series with the equation

$$\xi(\vec{s},t) = \frac{1}{2}\vec{a}_0(s) + \sum_{n=1}^{N_0} \vec{a}_n(s)\cos(n\omega t) + \vec{b}_n(s)\sin(n\omega t) \tag{2.18}$$

where the Fourier coefficients $\vec{a}_n$ and $\vec{b}_n$ were approximated by

$$\vec{a}_n = \sum_{m=1}^{M_0} \vec{A}_{mn} s^m \quad \text{and} \quad \vec{b}_n = \sum_{m=1}^{M_0} \vec{B}_{mn} s^m \tag{2.19}$$

and $\vec{A}_n$ and $\vec{B}_n$ are constants from tables 2.2 and 2.3 respectively, determined using Fourier analysis of beating cilia by Fulford and Blake [14]. They also defined a second set of constants to represent the cilia beat pattern in the presence of a mucus layer, shown in tables 2.4 and 2.5 . A superposition of the cilia beat profile in both of these cases is shown in figure 2.7.

The function in our program that defined the cilium boundary for each time step used this method to create a dense set of points that represent the cilium, and then selected a subset of

(a) (b)

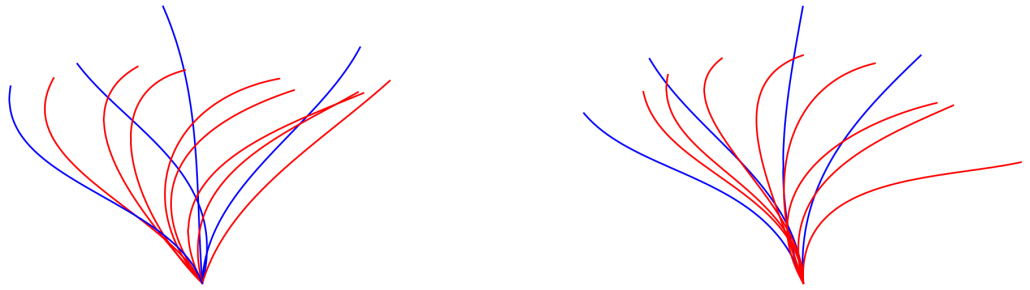

Figure 2.7: A superposition of the cilia beat profile used in our computational model when (a) there is no mucus present and (b) when there is mucus present.

$\vec{A}_{mn}$

n =	0	1	2	3	4	5	6
m = 1	-0.654	0.393	-0.097	0.079	0.119	0.119	0.009
	1.895	-0.018	0.158	0.010	0.003	0.013	0.040
m = 2	0.787	-1.516	0.032	-0.302	-0.252	-0.015	0.035
	-0.552	-0.126	-0.341	0.035	0.006	-0.029	-0.068
m = 3	0.202	0.716	-0.118	0.142	0.110	-0.013	-0.043
	0.096	0.263	0.186	-0.067	-0.032	-0.002	0.015

Table 2.2: Constants used to define Fourier coefficients for cilia beat profile in a single fluid.

$\vec{B}_{mn}$

n =	0	1	2	3	4	5	6
m = 1	0.0	0.284	0.006	-0.059	0.018	0.053	0.009
	0.0	0.192	-0.050	0.012	-0.007	-0.014	-0.017
m = 2	0.0	1.045	0.317	0.226	0.004	-0.082	-0.040
	0.0	-0.499	0.423	0.138	0.125	0.075	0.067
m = 3	0.0	-1.017	-0.276	-0.196	-0.037	0.025	0.023
	0.0	0.339	-0.327	-0.114	-0.105	-0.057	-0.055

Table 2.3: Constants used to define Fourier coefficients for cilia beat profile in a single fluid.

$\vec{A}_{mn}$

n =	0	1	2	3	4	5	6
m = 1	-0.449	0.130	-0.169	0.063	-0.050	-0.040	-0.068
	2.076	-0.003	0.054	0.007	0.026	0.022	0.010
m = 2	-0.072	-1.502	0.260	-0.123	0.011	-0.009	0.196
	-1.074	-0.230	-0.305	-0.180	-0.069	0.001	-0.080
m = 3	0.658	0.793	-0.251	0.049	0.009	0.023	-0.111
	0.381	0.331	0.193	0.082	0.029	0.002	0.048

Table 2.4: Constants used to define Fourier coefficients for cilia beat profile in a two layered fluid.

	$\vec{B}_{mn}$						
n =	0	1	2	3	4	5	6
m = 1	0.0	-0.030	-0.093	0.037	0.062	0.016	-0.065
	0.0	0.080	-0.044	-0.017	0.052	0.007	0.051
m = 2	0.0	1.285	-0.036	-0.244	-0.093	-0.137	0.095
	0.0	-0.298	0.513	0.004	-0.222	0.035	-0.128
m = 3	0.0	-1.034	0.050	0.143	0.043	0.098	-0.054
	0.0	0.210	-0.367	0.009	0.120	-0.024	0.102

Table 2.5: Constants used to define Fourier coefficients for cilia beat profile in a two layered fluid.

equally spaced boundary points that were used in the simulation for the each time step. The velocity of each point as the cilium beats was simply defined as the change in each points position between time steps. This process was repeated for each cilium included in the simulation, with alterations based on the position of each cilium and the phase step between adjacent cilia.

In our simulations we allowed cilia to move past each other so that we could investigate situations where the phase step between adjacent cilia was large without having to increase the cilium spacing. This means that boundary points from different cilia could move into very close proximity with one another, which could cause problems in our simulations since a single fluid node could be affected by several conflicting immersed boundary forces. To avoid this problem we included a function in our program that checked the full cilium array for boundary points that were separated by less than 1 lattice unit and deactivated one of those points. Cilia moving past one another also generated closed fluid regions in 2D simulations, but we avoided changes in the fluid density in these regions by allowing fluid to flow through the base of the cilia.

2.3 Modelling the Binary Fluid

The fluid that lines the epithelium is composed of two separate layers with different properties. The peri-ciliary liquid (PCL) that surrounds the cilia can be modelled as water where as the mucus layer is a polymer gel with visco-elastic properties [46]. There is also a distinct separation between the two layers that has been shown to be vital for effective cilia driven flow. We have taken all of these factors into account when developing our model of the binary fluid system.

2.3.1 Binary Fluid Modelling Techniques

In our model the two fluid components have separate population density values assigned to each node, meaning that each node essentially represents a mixture of the two fluids [28]. The behaviour of the two fluids at each node is calculated separately using the same lattice Boltzmann algorithm for each fluid component using different relaxation times for each component. We can represent the concentration of both components at each fluid node by calculating the order parameter (ϕ_c) such that

$$\phi_c = \frac{\rho^{(P)} - \rho^{(M)}}{\rho^{(P)} + \rho^{(M)}} \tag{2.20}$$

where $\rho^{(P)}$ and $\rho^{(M)}$ represent the density of of PCL and mucus respectively at a given fluid node [28]. The value of ϕ_c gives us some information on the ratio of the two components at a given fluid node such that $\phi_c = 1$ indicates that there is only PCL present, $\phi_c = -1$ indicates that there is only mucus present, and $\phi_c = 0$ indicates that there is an equal proportion of both components at that node. We note that in practice there should never be a region of fluid that contains solely one component as this can cause problems in the calculation of interaction forces [28].

External forces that affect a binary fluid node are split between the two fluids based on the ratio of the two fluid densities assigned to that node using the equation

$$\vec{F}^{(\sigma)} = \frac{\rho^{(\sigma)}}{\rho}\vec{F} \tag{2.21}$$

where σ denotes the fluid component. In our model we handled interactions between the fluid components using the Shan-Chen pseudo-potential method [28], where the interactions are represented by a force that can either attract different fluid components or repel them depending on whether the fluids are miscible or immiscible respectively. The Shan-Chen force acting on a single fluid component is a function of the density of the other component at adjacent fluid nodes. To avoid potential instabilities in the program we used a pseudo-potential of the fluid components rather than the actual density. The pseudo-potential is calculated by

$$\psi(\rho) = \rho_0\left[1 - \exp\left(\rho/\rho_0\right)\right] \tag{2.22}$$

with a reference density ρ_0 which was set to unity in our simulations. The Shan-Chen force was calculated using

$$\vec{F}^{(\sigma)}_{SC}(\vec{x}) = -\psi^{(\sigma)}(x) G_{PM} \sum_i w_i \psi^{(\tilde{\sigma})}(\vec{x} + \vec{c}_i \Delta t)\, \vec{c}_i \Delta t \tag{2.23}$$

where G_{PM} is a scalar value that dictates how miscible the two components are, and $\tilde{\sigma}$ denotes a different fluid component to σ. The Shan-Chen force was applied to both components in a similar way to an external force and separated the fluid region into two distinct layers such as in the pulmonary system. We specifically used the Guo forcing method [28] so that the behaviour of the interface between the two fluid components was independent of their viscosity. The Guo forcing method requires that we use the barycentric fluid velocity

$$\vec{u_B} = \frac{1}{\rho}\sum_\sigma \left(\sum_i f_i^{(\sigma)} \vec{c}_i + \frac{\vec{F}^{(\sigma)}_{SC} \Delta t}{2} \right) \tag{2.24}$$

as the equilibrium velocity of both components. The barycentric velocity is force corrected to make our simulations more accurate. Our model handled the interaction between the fluid components and the boundaries of the fluid region in a similar way. We calculated an interaction force between each fluid component and the boundary by

$$\vec{F}^{(\sigma)}_{SCB}(\vec{x}) = -\psi^{(\sigma)}(x) G_{\sigma B} \sum_i w_i B(\vec{x} + \vec{c}_i \Delta t) \vec{c}_i \Delta t \tag{2.25}$$

where $B(\vec{x} + \vec{c}_i \Delta t)$ is a binary function that indicates whether there is a boundary present at an adjacent node, and $G_{\sigma B}$ is a scalar value that dictates the strength of the interaction between the fluid component and the boundary [28]. In our model there were two types of boundary that we had to consider; the air boundary and the epithelium boundary, and each of these had a specific interaction value with each fluid component (G_{PA}, G_{PE}, G_{MA}, and G_{ME}). We chose these interaction values such that a mix of the two fluid components would not gather at the boundaries, which was likely to occur otherwise since there were no fluid components outside of the boundary to interact with. We used values of $G_{PE} = G_{MA} = 0$, $G_{PA} = G_{ME} = 4$ in our simulations so that the PCL is pushed away from the air boundary and mucus is pushed away from the epithelium boundary. This had the side effect of mucus wetting to the air boundary and the PCL wetting to the epithelium boundary.

For our simulations we modelled the PCL and mucus as immiscible fluids so that they would form two distinct layers with a well defined boundary between the two [28]. The transition between the two regions can be represented by the profile of ϕ_c across the boundary. By varying the value of G_{PM} we could control the sharpness of the transition between the two layers. For the results shown in figure 2.8 the fluids were initially separated into two layers such that $\phi_c = \pm 0.9$ for the PCL and mucus layers respectively. The layers were then allowed to relax to their equilibrium state before the transition profile was measured. We note that figure 2.8 also shows the wetting behaviour that was discussed previously. Based on this data we used a value of $G_{PM} = 6$ in our simulations to ensure that the transition between the two fluid layers was sharp while maintaining moderate interaction forces between the two layers. Using these methods we were able to run simulations of a two layered binary fluid where the cilia would only interact with the mucus layer during their active stroke, to represent the in vivo muco-ciliary transport system.

2.3.2 Visco-elastic Fluid modelling

To represent the visco-elastic behaviour of mucus we included a Maxwell elastic stress that acted only on the mucus component. The elastic stress would oppose the acceleration of the mucus while gradually dissipating based on the memory time τ_M [23]. The force that represents this behaviour in our model was calculated by

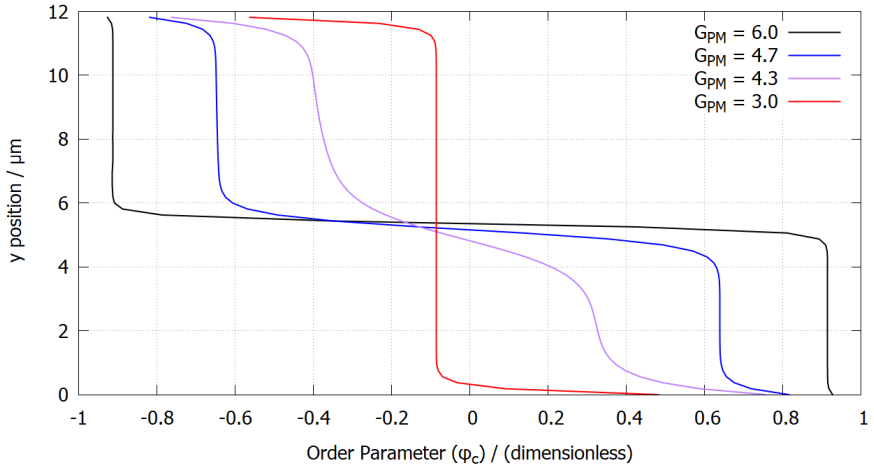

Figure 2.8: The profile of the order parameter (ϕ_c) showing the transition from the PCL to the mucus layer and how it varies with the value of G_{PM}.

$$\vec{F}_M(\vec{x},t+1) = \vec{F}_M(\vec{x},t)\left[1-\frac{1}{\tau_M}\right] + \Delta\vec{u}(\vec{x},t)\frac{\mu}{\tau_M} \tag{2.26}$$

where μ is the elastic coefficient and $\Delta\vec{u}(\vec{x},t)$ is the local difference in velocity between fluid nodes defined by

$$\Delta\vec{u}(\vec{x},t) = \sum_i w_i \left[\vec{u}(\vec{x}+\vec{c}_i,t) - \vec{u}(\vec{x},t)\right]. \tag{2.27}$$

The inclusion of this force made the mucus in our model behave as a visco-elastic fluid. To test that this behaviour is physically accurate we conducted some benchmarking simulations. We simulated a region of 96×96 fluid nodes with a periodic boundary in the x direction and reflecting boundaries in the y direction. The lower boundary was set to modify the fluid velocity at the wall with a periodic motion in the x direction that was proportional to $\cos(t/T)$. We selected parameters for the visco-elastic properties of our fluid to match those used by Ispolotov and Grant [23] such that $\mu = 0.3$ and $\tau_M = 46$, which means that the most suitable time period for our driving wall was also $T \approx 100$ [23]. We generated the results shown in figure 2.9 by measuring the fluid velocity for each full period of the oscillation ($u(y,t)\ \forall\ t = nT$), and taking the average of these measurements .

Our results clearly showed that the visco-elastic properties of the fluid caused it to oscillate in reaction to the oscillation of the driving wall, in agreement with the results of Ispolotov and Grant [23].

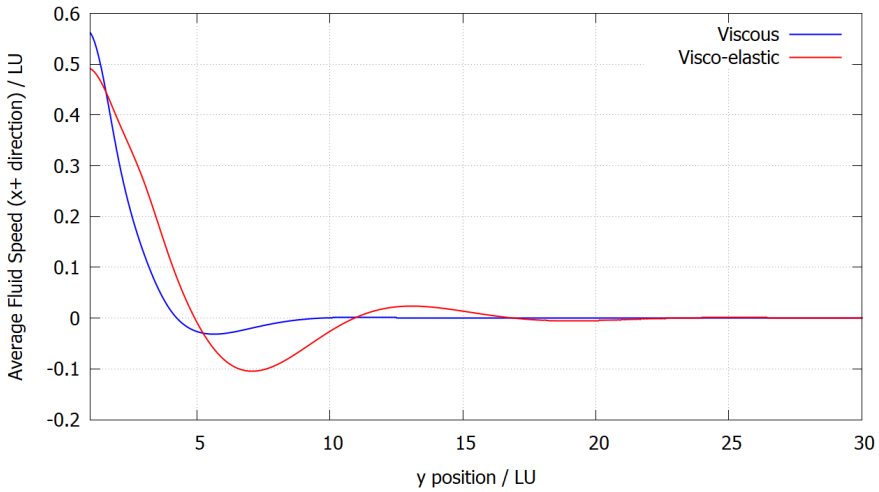

Figure 2.9: Average fluid velocity with distance from the driving wall, measured at each full period of the oscillation. Results are shown for viscous and visco-elastic fluids.

2.4 Measuring Fluid Flow Rate

The rate of fluid flow is a key characteristic of most of our simulation results. In our model we measured the flow rate as the flux across a fixed plane, or line in 2D simulations, that was perpendicular to the x axis. The average flux through the plane was calculated as

$$Q(x_p,t) = \frac{1}{YZ}\iint u_x(x_p,y,z,t)\,dy\,dz \tag{2.28}$$

where x_p is the position of the fixed plane and YZ is the cross section of the plane. The net fluid flow at a given time was calculated by

$$\tilde{Q}(x_p,t_n) = \int_0^{t_n} Q(x_p,t)\,dt. \tag{2.29}$$

To give a measure of the how far the fluid had flowed since the beginning of the simulation. Since our model works at the incompressible limit the actual position of the plane makes no difference to the flux through it. We used this method to measure fluid flow and flow rate in all of the simulations that we discuss in this project.

2.5 Boundary Conditions

For the lattice Boltzmann algorithm, it is important to have well defined boundary conditions that resolve the two major issues raised by the presence of non fluid boundaries. Namely what happens to population density that is streaming in the direction of the boundary, and how do we account for population density that would normally come from the direction of the boundary.

There are 3 different boundary conditions within our model that control the behaviour of fluid flow at each boundary. Each one deals with these issues in slightly different ways to represent different physical behaviours.

The epithelial boundary at $y = 0$ is treated as a non-slip bounce back boundary. Population density that would stream into the boundary is instead sent to the opposing side of the same fluid node. For example in Fig. 2.1 f_4 would stream to f_2 on the same node and f_7 would stream to f_5 in the same way. This means that fluid does not flow when in contact with the epithelium, hence "non-slip", and fluid that flows towards the boundary is sent back in the opposite direction, hence "bounce back".

The air boundary at the top of the fluid region is treated as a free-slip bounce back boundary. Population density that would stream directly into the boundary is handled in the same way as for the non-slip example, i.e. in Fig. 2.1 f_2 would stream to f_4 on the same node. The other population densities that would stream into the boundary are instead streamed in the opposite y direction while maintaining the same x direction, so f_5 would stream to f_8 on the same node and f_6 would stream to f_7. This means that while fluid flowing towards the boundary still bounces back, fluid is still able to flow while in contact with the boundary.

Both of these boundary types are implemented in our model using the mid-grid bounce back method. This is characterised by the position of the boundary at a distance of $0.5LU$ from the fluid nodes at the boundary, and that population density is reflected back from the boundary in a single time step [28].

The other boundaries of the system are treated as periodic boundaries so that population density that streams into the boundary is passed to the relevant fluid node on the opposing boundary as if it were an adjacent fluid node. This means that the fluid region that we have modelled explicitly behaves as if it were surrounded by identical fluid regions, creating a virtually infinite array of cilia generating fluid flow. To ensure that the cilium array is continuous we also apply the periodic boundary conditions to the boundary points that represent the cilia. When the positions of boundary points within the model are being calculated, if the position of the boundary point lies outside the fluid region it is altered so that its new position is offset from the opposing periodic boundary. This means that a cilium which extends out of the fluid region emerges from the opposite side as if it were originating from outside of the fluid region. A graphical representation of this behaviour is shown in figure 2.10. We note that the interaction of the boundary points with the periodic boundary combined with with the deactivation of boundary points that are too close together means that there is a minimum fluid region size imposed on our model. This is because we cannot allow a cilium to be close enough to both periodic boundaries that it could possibly interact with its self, as this would mean that all of the boundary points on that cilium would be deactivated. This means that for a cilium length of 6μm our fluid region must measure at least 12μm in the x dimension.

Implementing the periodic boundary conditions in this way meant that we could simulate the

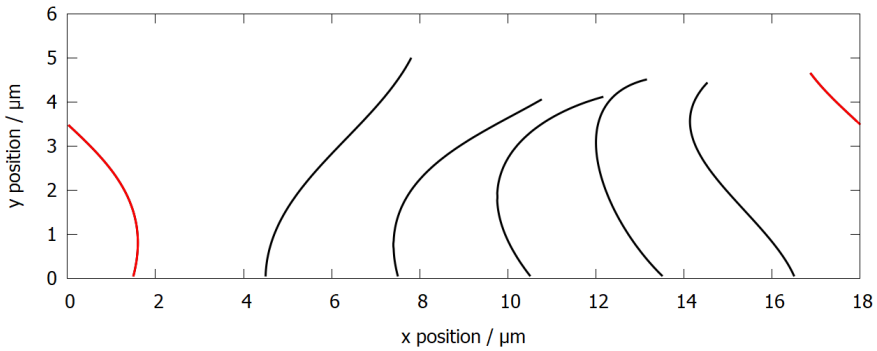

Figure 2.10: Example of a cilium passing through the periodic boundary in our model.

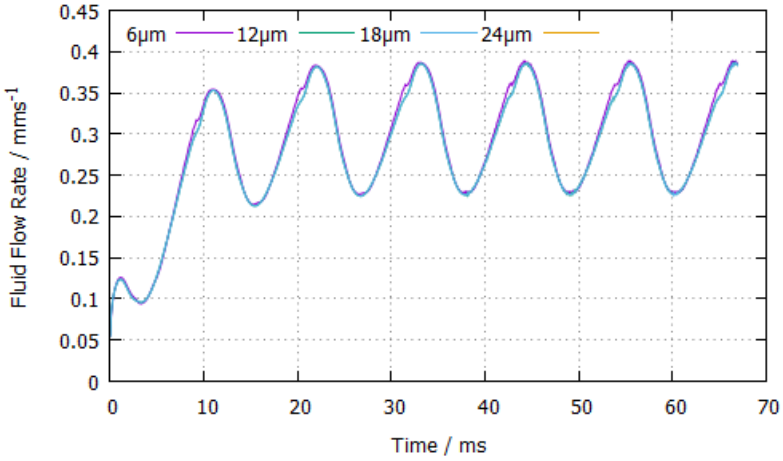

Figure 2.11: Results from different fluid region sizes with the same metachronal wavelength and cilium spacing. Showing minimal variation of flow behaviour when the x dimension of the fluid region is increased.

Table 2.6: Fluid flow rate for different fluid region sizes

Fluid Region Extent / μm	Fluid Flow Rate / mms^{-1}
6	0.3083
12	0.3039
18	0.3039
24	0.3039

behaviour of larger fluid regions while only explicitly modelling a small fluid region with a small number of cilia. As such, our model is able to generate a continuous metachronal wave in the cilium array so long as the x dimension contains a whole number of metachronal wavelengths. We conducted a set of simulations to confirm that this has a minimal effect on the results of the simulations.

Table 2.7: Cilia Simulation Parameters

Parameter	Simulation	Observed (from Literature)
Cilium length (L) / μm	6	5-7 [15]
cilium spacing (S) / μm	0.75-3	0.8 [15]
Fluid Height (H) / μm	12	12-18 [26]
Beat frequency / Hz	15	10-16 [13]
Metachronal wavelength (λ_M) / μm	1.5-18	6.5-13.1 [15]
Visco-elastic memory (τ_M) / s	6	1-10 [30]

Figure 2.11 shows results from four simulations that were run with the same phase step ($\Delta\phi = \pi/3$) and cilium spacing ($S = 1\mu m$). Each simulation had a different x dimension, and our results confirmed that the fluid flow behaviour for each simulation was virtually identical. Further analysis of these results showed that the fluid flow rate is also virtually unaffected by the variation of the x dimension, as shown in table 2.6.

2.6 Simulation Parameters

We have selected specific parameters for our simulations to ensure that our model is representative of the in vivo system. Parameters such as the cilium length, cilium spacing and fluid height have been well documented through electron microscopy in the literature [15, 26]. Some of the mechanical parameters such as the cilia beat frequency and metachronal wavelength are less well defined in the biological system [13, 15]. We have selected a beat frequency to optimise cilia driven fluid flow, and a range of metachronal wavelengths that allow us to investigate how this parameter affects fluid flow. The major physical parameters are summarized in table 2.7.

2.7 Convergence Testing

The scale of the pulmonary cilia system relative to the kinematic viscosity of water ($\nu \approx 8 \times 10^{-7} m^2 s^{-1}$) means that the Reynolds number is very small ($Re \approx 3 \times 10^{-3}$), but achieving significant and accurate results from our model with this Reynolds number would be infeasible because the time step must be decreased in proportion with the Reyolds number. When working with low Reynolds numbers it is often possible to use a numerical Reynolds number that is slightly higher than the physical Reynolds number, provided that the important properties of the fluid are still representative of the physical system [28]. We conducted a series of convergence tests to determine a suitable Reynolds number that would allow us to run simulations quickly without sacrificing the validity of our model. We found that simulations using $Re = 1$ ($\nu \approx 2.4 \times 10^{-9} m^2 s^{-1}$) display identical behaviour with comparable flow rates to those given by simulations using $Re = 0.003$ ($\nu \approx 8 \times 10^{-7} m^2 s^{-1}$), with a significant reduction in run time.

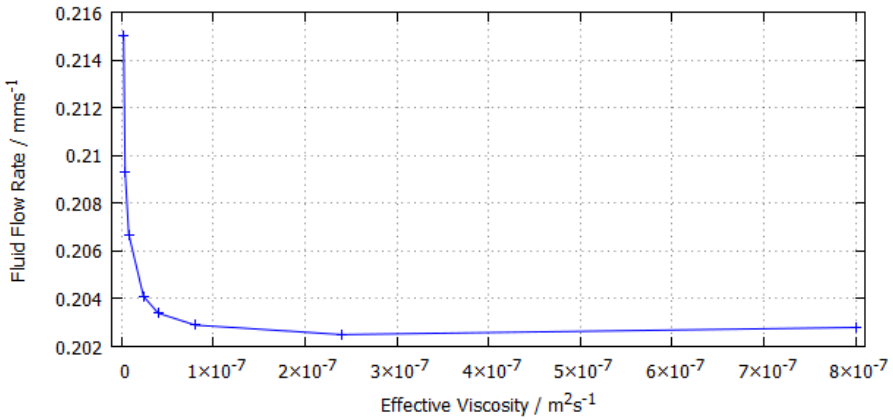

Figure 2.12: Results from convergence tests to justify using a numerical Reynolds number $Re = 1$ ($\nu \approx 2.4 \times 10^{-9} \mathrm{m}^2\,\mathrm{s}^{-1}$) to represent the biological system where $Re \approx 0.003$ ($\nu \approx 8 \times 10^{-7} \mathrm{m}^2\,\mathrm{s}^{-1}$).

Results from these convergence tests are shown in figure 2.12. Based on the results of these convergence tests, we used a value of $Re = 1$ in all of our simulations unless otherwise stated.

2.8 Program Outline

The development of our simulation program was a major part of this research project, and all of the results that we present here have been generated using this program. Because it plays such an important roll in our research, we provide a summary of the program in this section. The full code with documentation is also available through Github [18]. The summary presented here represents the case where there are two immiscible fluid components present in a 3D simulation.

For each time step of the simulation the program defines the cilia beat profile and runs through the steps of the lattice Boltzmann algorithm before calculating interaction forces between the fluid components and the external force from the immersed boundary. The main iteration loop is summarised in algorithm 1. We initialise the system at the beginning of each simulation so that the fluid is stationary with uniform density and each fluid node is in its equilibrium state.

We define the form of the cilia boundary for each time step using the `DefineBoundary` function. This function uses the number of cilia (c_{num}), the spacing between cilia (c_{space}) and the cilium length (`LENGTH`) to calculate the positions of a set of boundary points that represent the cilia for each time step. The shape of each cilium boundary is calculated using equations 2.18 and 2.19. We ensure that the spacing of these boundary points is one lattice unit to maximise the accuracy of the simulation [36]. This function also uses the position of the boundary points for the previous time step to calculate the velocity of each boundary point.

The `BoundaryCheck` function shown in algorithm 2 performs a proximity check for all boundary points to ensure that no two points are within one lattice unit of each other. We first define a region for each cilium that gives an over estimate of the area that the cilium will pass

Algorithm 1: Main iteration loop

```
Initialise fluid nodes to equilibrium
ρ = 1 ∀ fluid nodes
u = 0 ∀ fluid nodes
Equilibrium(ρ^P, u^P, ρ^M, u^M) ⟶ f_0^P, f_0^M
f^P = f_0^P ∀ fluid nodes
f^M = f_0^M ∀ fluid nodes

for it:0 → T do
    Define the cilia boundary for this time step
    DefineBoundary(it, c_num, c_space, length) ⟶ s, u^S

    Deactivate boundary points that are too close to one another
    CheckBoundary(s, c_space, LENGTH) ⟶ s, ϵ

    Execute lattice Boltzmann algorithm
    Equilibrium(ρ^P, u^P, ρ^M, u^M, Force) ⟶ f_0^P, f_0^M, F
    Collision(f_0^P, f^P, f_0^M, f^M, F) ⟶ f_1^P, f_1^M
    Streaming(f_1^P, f_1^M) ⟶ f^P, f^M
    Macro(f^P, f^M) ⟶ ρ^P, ρ^M, u^M, ρ, u

    Calculate forces from fluid component interactions and
     visco-elasticity
    BinaryForces(f^P, f^M, u^M, it) ⟶ force^P, force^M, force^E

    Calculate forces from immersed boundary
    Interpolate(ρ, u, s, u^S) ⟶ F^S
    Spread(F^S, u^S, ϵ) ⟶ force^S

    Apply forces to fluid and record flux
    Forces(ρ, force^P, force^M, force^E, force^S) ⟶ u, Force, Q
```

through during a full stroke, we call this the sweep area. We then compare the positions of each boundary point belonging to cilia that have intersecting sweep areas. If any of these points are within one lattice unit of one another then one of those points is deactivated by setting the boolean variable ϵ to zero. This function also handles boundary points that cross periodic boundaries and shifts their positions to the equivalent location on the other side of the fluid region.

The `Equilibrium` function calculates the equilibrium population density at each fluid node based on a discretised form of equation 2.3. We have parallelised this function so that each thread calculates the population densities at a single fluid node, which means that the number of threads is equal to the number of fluid nodes in the simulation. Similarly the `Collision` function uses a discretised form of equation 2.4 to calculate the population densities after relaxation of the

Algorithm 2: BoundaryCheck function

```
Function launches a thread for each boundary point

Handle boundary points that lie outside of the fluid region
(dimensions: XDIM*YDIM*ZDIM)
if s[x] > XDIM then
    s[x]-= XDIM

if s[x] < 0 then
    s[x]+= XDIM


Number of cilia that potentially intersect
r_max = 2 * LENGTH/c_space

Check cilia in range
for r : 1 → r_max do
    Check along cilia length
    for l : 0 → LENGTH do
        Check for intersection in x on same row
        if abs(s_m[x] − s_l[x]) < 1  AND  s_m[z] = s_l[z] then
            x_close =TRUE

        if abs(s_m[y] − s_l[y]) < 1  AND  s_m[z] = s_l[z] then
            y_close =TRUE

        if x_close  AND  y_close then
            ϵ = 0
```

fluid. However, we have parallelised this function so that each thread performs this calculation for an individual population density. This means that the function launches with a number of threads equal to the total number of population densities in the simulation.

The `Streaming` function controls the movement of population densities between adjacent fluid nodes based on the direction associated with each population density. For the majority of fluid nodes this calculation is quite straight forward, but for calculations at the edges of the fluid region the boundary conditions described in section 2.5 have to be taken into account. This means that the calculation performed by the function depends on both the position of the fluid node and the population density being streamed. We calculate the position of the fluid node within the region using the unique index of the fluid node. If the node does not lie on a boundary then the streaming calculation is done as normal, otherwise the type of boundary is identified by the position of the node and the calculation associated with that boundary is performed. In the case

of the free slip and non-slip boundaries this simply means that we assign a new direction to the population density. For the periodic boundary we calculate the position of the destination node at the opposite end of the fluid region and the population density is streamed to this node as if it were adjacent to the origin node.

The `Macro` function calculates the macroscopic variables associated with each fluid node using equations 2.5 and 2.6. We calculate the density of each fluid component separately and take the sum of the two as the total fluid density at each node. The velocity is calculated prior to the application of external forces so that it can be used to calculate immersed boundary forces. We also calculate the velocity of the mucus component separately so that it can be used to calculate visco-elastic forces.

Each step of the lattice Boltzmann algorithm is performed for the two fluid components separately and interactions between the two are handled by the `BinaryForces` function. We calculate the force between fluid components using equation 2.23, and in this function we also use equation 2.26 to calculate the visco-elastic force that is applied to the mucus component of the fluid. For each fluid node we calculate the Shan Chen force affecting both fluid components by finding the concentration of the other component on the adjacent fluid nodes. The position of the adjacent fluid node dictates the direction of the resulting force. This interaction obeys the periodic boundary condition so that the fluid nodes at the boundary are affected by the fluid nodes on the opposing boundary in a similar way to the `Streaming` function. At the air and epithelial boundaries, the interaction between fluid components is replaced by a specific interaction between each fluid component and the material at the boundary.

The `Interpolate` function calculates the force at each boundary point using equation 2.8 and the smoothed delta function defined by equation 2.10. This force is then used in the `Spread` function to calculate the force that the boundary point exerts on the surrounding fluid nodes using equation 2.11.

The `Forces` function collects all of the forces that have been calculated in to a single external force that is applied to the fluid nodes and used to modify the barycentric velocity using equation 2.24.

2.9 Runtime Optimisation

We have optimised our simulation program using Nvidia Visual Profiler [35], and with help from the Research Software Engineering group at the University of Sheffield. Visual Profiler offers guidance on several aspects of program optimisation for GPU execution.

The first thing that we had to consider when optimising our program was the occupancy of the processors on the graphics card, and how efficiently the processes to be executed can be divided into blocks of parallel threads. In the case of the lattice Boltzmann algorithm this is directly linked to the dimensions of the fluid region, and in our program this is linked to the length of a

single cilium since we have set the fluid region height to be two cilium lengths. For this reason we set the cilium length to ensure that the dimensions of the fluid region and hence the number of fluid nodes in the model is divisible by 32. This is important because the size of a block should always be a multiple of 32, so our fluid nodes can be divided equally between blocks and no blocks are launched with low occupancy.

Another key area for optimisation in our program is divergence. Divergence occurs when one or more threads within a block is performing a different task to all of the other threads, which would mean that the other threads within that block have to wait for that one thread to complete it's task before the block can finish running and another block can run. This is quite likely to occur in our program where boundary points interact directly with fluid nodes because the form of that interaction depends on the distance between the fluid node and the boundary point, as shown in equation 2.10. To reduce the effect of divergence in this situation, we have altered the algorithm for calculating $\tilde{\delta}_a$ so that rather than performing one of three calculations each thread performs the same calculation

$$\tilde{\delta}_a = A\left(B + C\sqrt{-3D^2 + 1}\right) \tag{2.30}$$

where the constants A, B, C, and D are chosen based on the distance between the fluid node and the boundary point. This means that every thread performs a very similar task but the results are still individual to each fluid node, and the time lost to divergence is minimised.

We were able to further optimise our code through the use of multi streaming. The idea behind multi streaming is that functions or kernels that are independent of one another can be executed at the same time so that when one kernel is performing memory operations the other can be performing computations on the same graphics card. This can reduce latency that is caused by large memory operations taking up GPU resources. In our program the kernels that calculate the positions and velocities of boundary points are independent of the majority of kernels that calculate fluid behaviour, since these two aspects of the program only interact when the external force acting on the fluid is being calculated. We assign the boundary point and fluid node kernels to different streams so that the boundary point calculations can be performed while the large amount of data that represents the fluid nodes is passed to and from the GPU.

2.10 Summary

In this chapter we have explained all of the computational methods that we have used in our project. This includes the equations used in the immersed boundary lattice Boltzmann algorithm, which forms the backbone of our computational model. We have also discussed our use of the two relaxation time (TRT) method to simulate fluid flow at very low Reynolds numbers [28].

The specifications of our numerical model include results from our simulations of flow past a cylinder, which we have used as a benchmark of our model against experimental and simulation

results from the literature [10, 32, 36]. In these simulations, we were able to recreate the closed wake behaviour that is well documented for intermediate Reynolds numbers and the emergence of a Von Karman vortex street at higher Reynolds numbers.

Our method of modelling the cilium beat profile using a truncated Fourier series [14] is explained, including the alterations made to the beat profile to account for the presence of a second fluid layer. We have also given details of how we were able to model a binary fluid by performing the majority of the lattice Boltzmann calculations for each fluid component separately, and calculating the interaction forces between the two components using the Guo forcing method. A Maxwell elastic stress was added to the mucus component to simulate the visco-elastic properties of mucus in vivo [23]. With results from a benchmarking simulation of flow induced by an oscillating boundary to validate the visco-elastic behaviour of the fluid.

We have briefly discussed how the fluid flow rate was calculated in our simulations. We outlined the boundary conditions used in our model and how we were able to use periodic boundary conditions to explicitly model a small number of cilia to represent a large cilium array. We have given details of the key parameters that we have used in our model, and discussed our use of a numerical Reynolds number to simulate fluid flows at very low Reynolds numbers [28]. Including the results of convergence tests to justify the numerical Reynolds number that we chose to use.

We have given an overview of our simulation program and the specific functions of each kernel that the program launched during a simulation. This includes some pseudo code that gives details of the variables that are input and output for each kernel. This also includes a description of each kernel and how they relate to the immersed boundary lattice Boltzmann (IBLB) algorithm. We have also given some examples of how our program has been optimised for implementation on a GPU.

3

SINGLE CILIUM BEHAVIOUR

In this chapter we present results from a study of the characteristics of fluid flow generated by a single cilium in a large fluid region. We show the shape of the fluid velocity profile in both the x and y direction generated by 2D simulations, and how these profiles vary depending on the Reynolds number of the model. We quantify the velocity profile by its characteristic length (λ) by representing the velocity profile in the x direction as an exponential decay with the distance from the cilium, and determine the explicit relationship between the characteristic length and the Reynolds number.

We explain how our model is altered to simulate the presence of a mucus layer with higher viscosity and visco-elastic properties. Showing how the presence of the mucus layer affects the observed flow behaviour, and highlighting some of the new properties of the fluid velocity profiles caused by the presence of a visco-elastic fluid layer.

3.1 Fluid Velocity profiles

We have carried out a series of simulations to determine how the fluid speed varies depending on the distance from a beating cilium. For the velocity profile in x we measured fluid speed on a line parallel to the x axis at the height of the cilium tip when the cilium was fully extended. This meant that we were able to observe the velocity profile in x due to the beating cilium without interference from the boundaries at the top and bottom of the fluid region. For the velocity profile in y we we measured the fluid speed on a line parallel to the y axis at the position of the cilium base. Meaning that we could record the vertical velocity profile that was generated by a single cilium in a large fluid region.

We note that all of the simulations presented in this section were carried out in 2D with a single cilium in a fluid region with dimensions $48\mu m \times 24\mu m$. We used the periodic boundary conditions described in section 2.5 to ensure that the fluid could flow freely in the x direction. This means that our simulations actually represented multiple cilia but we have used a very large cilia spacing of $48\mu m$ (8 cilium lengths) to ensure that the interactions between the cilia are

(a)

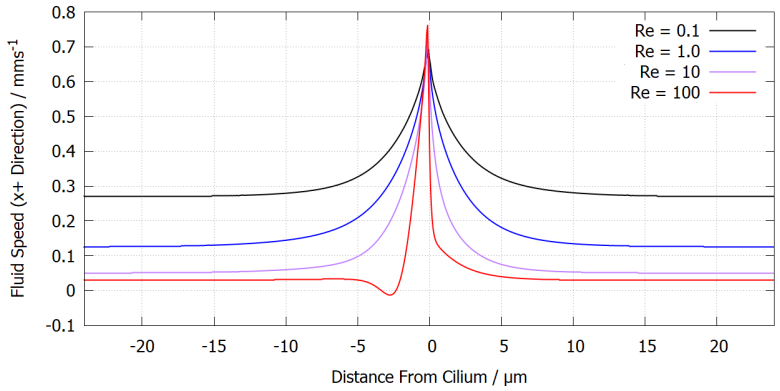

(b)

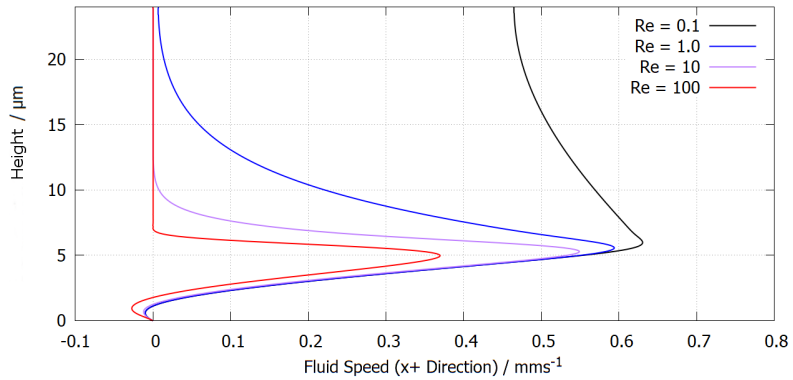

Figure 3.1: The instantaneous velocity profile in (a) the x direction at the height of the cilium tip and (b) the y direction at the position of the cilium base, and how these profiles change with the Reynolds number. We observe that the profile in x is close to an exponential function for small Re and deviates from this shape as Re increases.

minimised. We measured the fluid speed when the cilium is mid way through the active stroke, extended vertically and moving rapidly through the fluid.

The vertical velocity profile that we observed, shown in figure 3.1b, was similar to observations in the literature [22, 45]. With a peak in fluid speed around the height of the cilium tip (6µm) and a gradual decrease in fluid speed above this height. We observed that the horizontal velocity profile generated by the cilium could be represented by an exponential decay with distance from the cilium. This velocity profile is shown in figure 3.1a for a range of Reynolds numbers. We characterised the velocity profile with the equation

$$v_x(\Delta x) = U_c e^{-|x-x_c|/\lambda} + u_0 \tag{3.1}$$

where x_c is the position of the cilium base, λ is the characteristic length of the exponential decay, U_c is the cilium tip speed and u_0 is the residual fluid speed. We note that equation 3.1 includes only the x component of the velocity profile since this is the only direction that net flow is possible

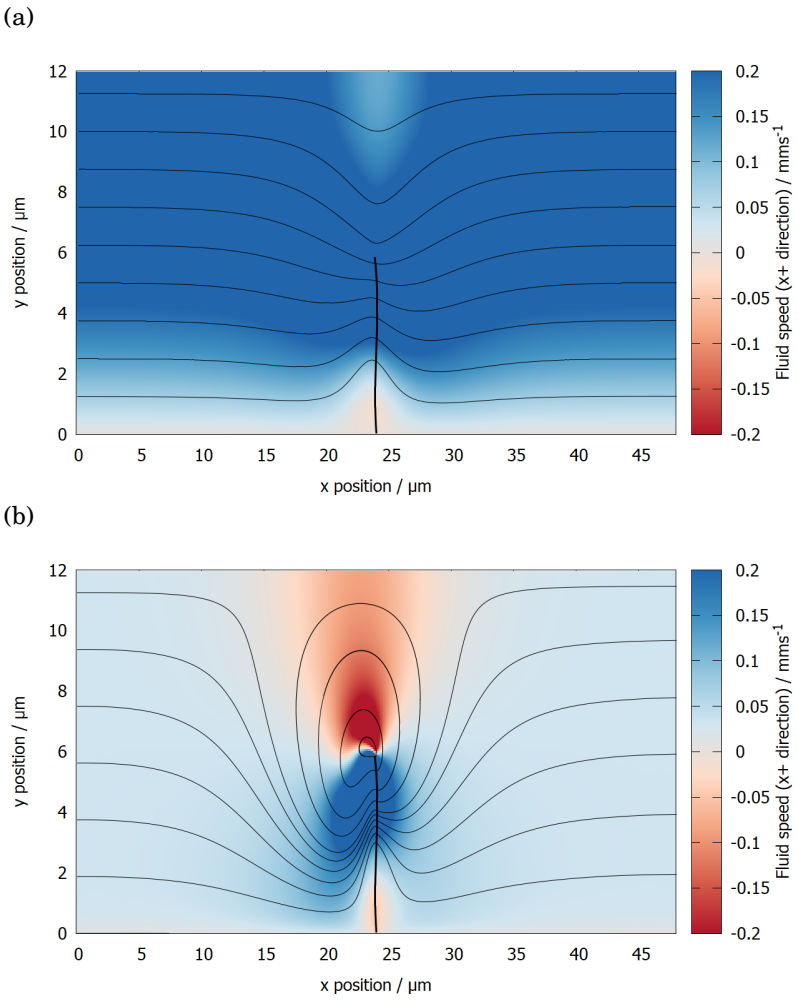

Figure 3.2: Streamline plots of flow around the cilium tip during the active stroke for (a) $Re = 0.1$ showing almost laminar flow and (b) $Re = 100$ showing rotational flow in the wake of the cilium tip.

in our model. This behaviour is due to the dissipation of energy within the fluid caused by viscous drag and the presence of rotational flow in the fluid, and as such the shape of the velocity profile varies with the Reynolds number (Re) of our model [29]. By fitting our exponential function to the velocity profile for each value of Re we were able to quantify the characteristic length of the velocity profile in each case. As Re was increased the velocity profile changed in two significant ways. The characteristic length (λ) decreased and the residual fluid velocity far from the cilium also decreased. We note that when $Re > 10$ we observed the emergence of a vortex in the wake of the cilium tip. This meant that the exponential function that we used to represent the velocity profile was not valid for larger values of Re ($Re > 10$). We have visualised this phenomenon more clearly by plotting at the stream lines around the cilium tip for both small and large values of Re as shown in figure 3.2.

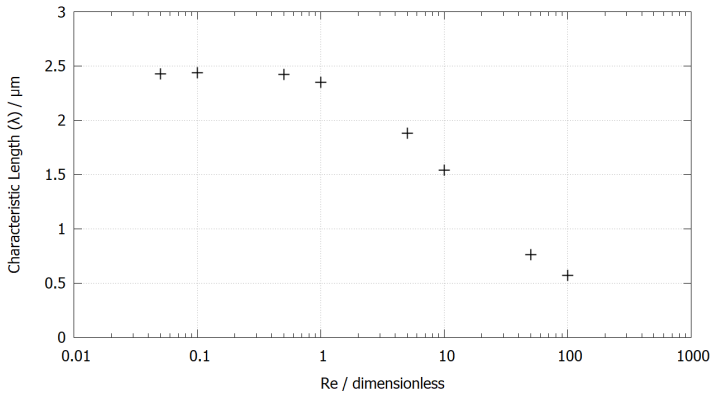

Figure 3.3: The relationship between Re and the characteristic length (λ) of the observed velocity profile. The characteristic length converges to a value of $\lambda = 2.44\mu m$ (0.407 cilium lengths) for $Re \leq 1$. We note that the exponential fit becomes less representative of the velocity profile as Re increases.

Our results are shown in figure 3.3. We see from this data that λ converged for small Re to a value of $\lambda = 2.44\mu m$ (0.407 cilium lengths). The shape of the relationship between λ and Re implied that what we observed was a transition from viscous to inertia dominated regimes. Assuming that the transition could be represented by a sigmoid profile of the form

$$S_f(x) = \frac{A}{B\sqrt{C + Dx^2}} \tag{3.2}$$

we obtained the charcteristic lengths of each regime where the viscous regime was represented by a characteristic length of $\lambda = 2.44\mu m$ (0.407 cilium lengths), and the inertia dominated regime was represented by $\lambda \approx 0.3\mu m$ (0.07 cilium lengths). It should be noted that the value of λ for the inertia dominated regime is an extrapolation due to the limitations of our fit at high Re.

3.2 Binary Fluid Velocity profiles

When we introduced a visco-elastic fluid layer into our simulations there were several changes to the model that had to be taken into account. First of all we altered the cilium beat profile to the form shown in figure 2.7b in agreement with the observations of Fulford and Blake [14]. We set the height of the mucus layer such that the cilium only interacted with the mucus layer during its active stroke as shown in figure 3.4. The transition between the two layers was gradual, as can be seen in figure 3.4, and the transition region had a thickness of 8-10 lattice units. The mucus layer also had visco-elastic properties that were represented in our model by a Maxwell elastic stress between adjacent fluid nodes as described in section 2.3.2 [23].

Because of these changes, the behaviour of the fluid in the presence of a single beating cilium was somewhat different. The velocity profile in the x direction from our binary fluid simulations changed significantly, and figure 3.5a shows that the velocity profile could no longer be expressed

(a) (b)

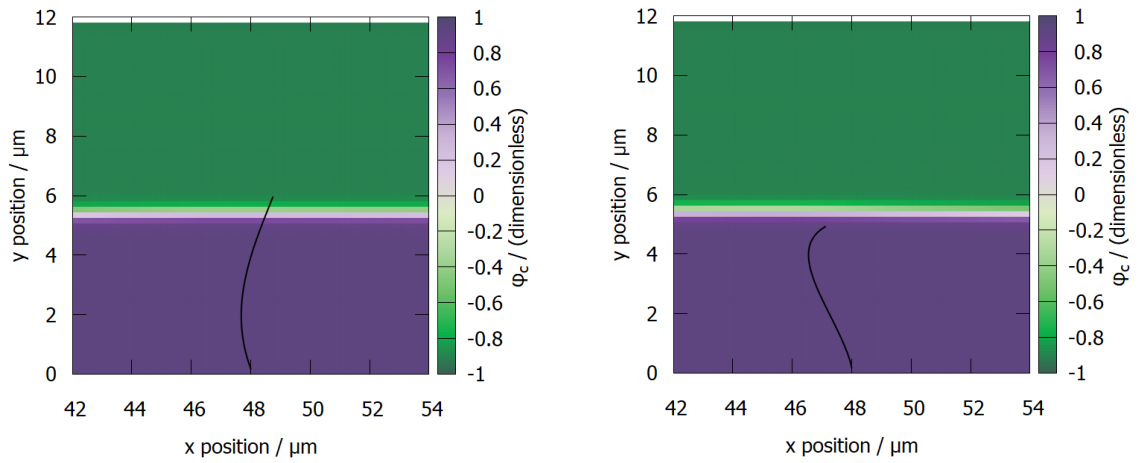

Figure 3.4: (a) An example of the cilium penetrating the mucus layer during the active stroke and (b) passing under the mucus layer during the recovery stroke.

as an exponential function of the distance from the cilium. We note that due to the position of the cilium tip during the active stroke (shown in figure 3.4a) the velocity profile in the x direction was measured only in the mucus layer.

Figure 3.5b shows that the velocity profile in the y direction had a shape consistent with the higher viscosity of the mucus layer and the slower cilium beat. A similar profile for fluid speed in a two layered fluid was observed by Chateau et al. [6]. The transition region between the two fluid components is plotted for clarity. The velocity profile during the recovery stroke, plotted in figure 3.5c, showed some shear banding in the transition region. This was amplified by the visco-elastic properties of the mucus layer resulting in similar behaviour to that observed in simulations of Couette flow in visco-elastic gels [31]. In our simulations this behaviour emerges due to the large disparity between the shear rate close to the cilium tip, and the shear rate in the mucus layer. This generates step between the high and low shear rates that propegates up through the transition region over time. The step in shear rates causes a recoil flow in the mucus layer, which causes a small region of fluid to flow in the opposite direction.

3.3 Summary

We have conducted a study of the behaviour of fluid driven by a single beating cilium. From our data we have calculated the instantaneous velocity profiles associated with the beating cilium and shown that the profiles generated by our simulations are consistent with those observed in the literature [22, 45]. By fitting an exponential function to the observed velocity profile in the x direction, we have quantified the velocity profile by its characteristic length λ. We have also

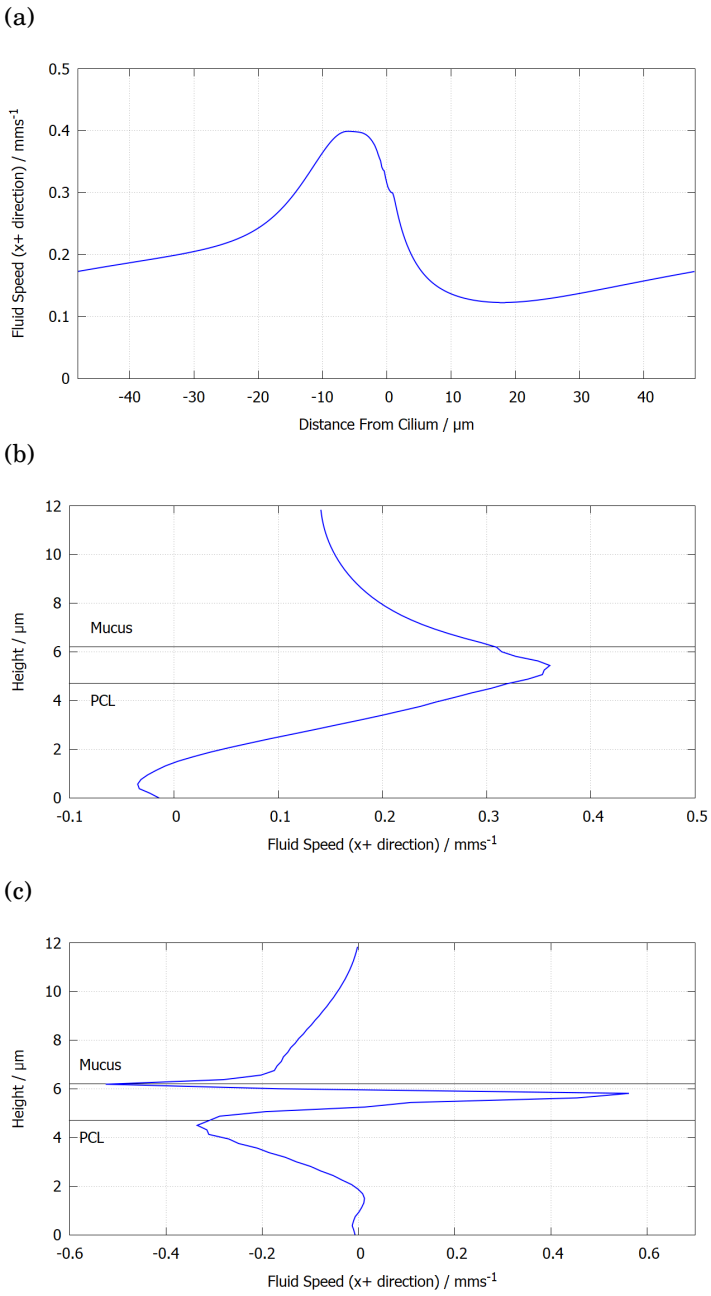

Figure 3.5: (a) Instantaneous velocity profile in the x direction with a visco-elastic mucus layer present in the model. (b) Instantaneous velocity profile in the y direction for a binary fluid during the active stroke. (c) Instantaneous velocity profile in the y direction for a binary fluid during the recovery stroke. The transition region between the two fluid layers is also shown.

shown how this characteristic length changes with the Reynolds number of the model, and that the value converges to $\lambda = 2.44\mu$m for low Re.

By introducing a second fluid layer we have shown that the higher viscosity and visco-elastic properties of the mucus layer mean that the velocity profile can no longer be represented by an exponential function. We have also observed the presence of shear banding in the transition between the two fluid layers.

This study helps us to understand how fluid flows around a beating cilium, and the results from this work can be used to further our understanding of how fluid flows in the presence of a large array of beating cilia and construct an analytical model of the system.

4

Metachronal Wavelength and Fluid Flow Rate

In this chapter we present the work published in Hall and Clarke (2020) [19] on the relationship between the fluid flow rate driven by an array of beating cilia, and the clustering of cilia in the array due to metachronal beating.

As noted in chapter 1 experimental observations of pulmonary cilia have shown that an array of cilia do not beat in synchrony, but there is a phase step between the beat cycles of adjacent cilia [13]. In large arrays of cilia this behaviour forms a metachronal wave that travels through the cilium array. In vitro the metachronal wave has been observed to be antiplectic, moving in the opposite direction to the active stroke of the cilia [14], as opposed to a symplectic wave that would move in the same direction as the active stroke. The wavelength of this metachronal wave is directly related to the size of the phase step between adjacent cilia. Previous studies in this area have identified that a cilium array that beats with a metachronal wave can generate fluid flow much more effectively than an array that beats in synchrony, and that there is a distinctive relationship between fluid flow and metachronal wavelength [6, 11]. In the work of Chateau et al. [6] they postulate that the higher fluid flow generated by antiplectic cilia beating is due to the clustering of cilia during the recovery stroke, which would minimise their impact on fluid flow. This is explained in greater detail in section 1.1.2.

The work that we present in this chapter seeks to expand on this idea by investigating the role played by cilium spacing on this behaviour [15], and then quantifying the relationship between metachronal wavelength and fluid flow rate with an analytical model.

We first present our observations on the variation of fluid flow with metachronal wavelength, and how this relationship changes depending on the cilium spacing. We then derive the analytical model that we have used to quantify the area of fluid that is free to flow in the cilium array. We show that the results from our analytical model and numerical simulations indicate a strong correlation between free area and fluid flow rate, and that this correlation is independent of cilium spacing. We then show results from a further investigation of this behaviour with the inclusion of a visco-elastic mucus layer.

4.1 Observations

We observed that the fluid flow rate was dependent on the phase step and by varying $\Delta\phi$ we could change the rate of fluid flow as shown in figure 4.1a. We note that increasing $\Delta\phi$ also caused an oscillation in the flow rate with time, due to the time delay between the active stroke of each cilium. Our results also indicated that the cilium array was most effective at driving fluid flow when the tips of the cilia were more widely spaced during their active stroke. As an example the flow rate recorded for $\Delta\phi = \pi/6$ was significantly higher than for $\Delta\phi = \pi/12$, and there was a visible difference between the cilia spread in these two cases as shown in figures 4.1b and 4.1c.

An extreme case of this behaviour occurred when $\Delta\phi = 23\pi/12$. Figure 4.2 shows that in this case the cilia were clustered together during the active stroke and spread out during the recovery stroke. This meant that the recovery stroke could drive the fluid more effectively than the active stroke, and the resulting fluid flow was in the opposite direction to what we expected. We note that similar behaviour has been observed in the literature [6, 11].

By running simulations for the full range of phase step values ($0 \leq \Delta\phi \leq 2\pi$) we were able to see the relationship between phase step and fluid flow rate. The data presented in figure 4.3 shows that this relationship had a number of distinctive features. The clearest feature was that fluid flow rate associated with synchronised cilia beating ($\Delta\phi = 0, 2\pi$) was significantly lower than the flow rate associated with most other $\Delta\phi$ values. We have explored this particular behaviour in more detail in section 5.1. Local minima in fluid flow rate were also associated with phase step values that correspond with partial synchrony, where a cilium in the array is synchronised with another nearby cilium. For example when $\Delta\phi = \pi$ cilium n is synchronised with cilia $n \pm 2$, and when $\Delta\phi = 2\pi/3, 4\pi/3$ cilium n is synchronised with cilia $n \pm 3$. Our data also showed an asymmetry between antiplectic metachrony ($\Delta\phi < \pi/2$) and symplectic metachrony ($\Delta\phi > \pi/2$) which was consistent with data from the literature [6, 11].

We have also observed that the relationship between phase step and flow rate changes significantly with variations in cilium spacing. Results for a range of cilium spacings ($0.75, 1.5, 2.25, 3\mu m$) are shown in figure 4.3. These results showed an overall increase in the fluid flow rate as the cilium spacing is reduced, which is consistent with a higher density if cilia driving fluid flow. The results also indicated that the effects of metachrony that we have observed have a greater effect on fluid flow for smaller cilium spacings. This highlighted the decrease in fluid flow caused by partial synchrony in the cilium array.

We have also compared the fluid flow rate from 2D and 3D simulations for the same phase step to show that both models represent the same behaviour, as we can see in figure 4.4a. The only major difference between the two results was that the flow rate in the 3D case was slower than in the 2D case. This was as expected since the 2D model represented infinite rows of cilia with no space between them, where as the 3D model included space between the rows of cilia which reduced the effectiveness of each cilium stroke. This consistency extended to the full range of $\Delta\phi$ values such that the relationship between phase step and flow rate was the same for 2D

(a)

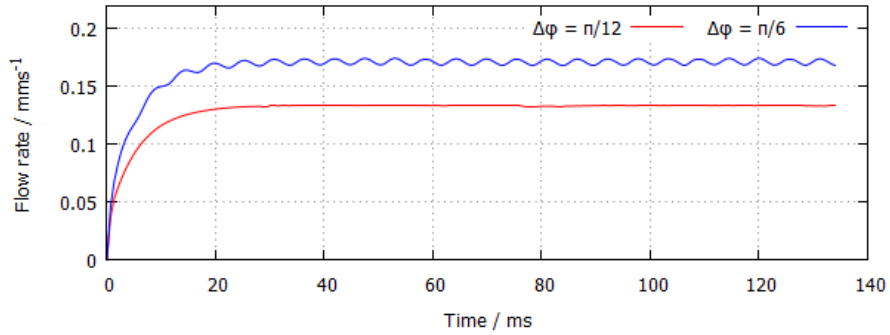

(b)

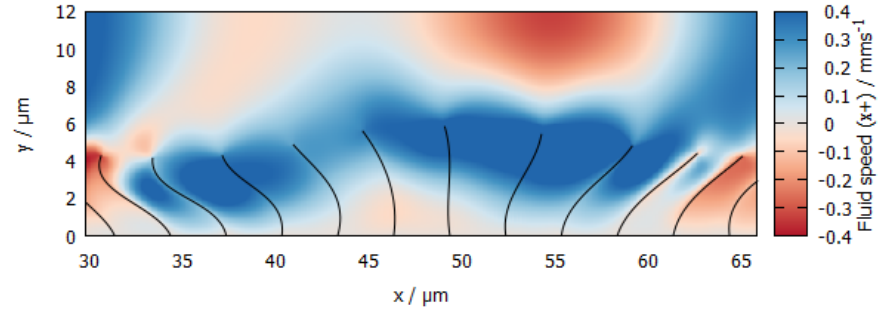

(c)

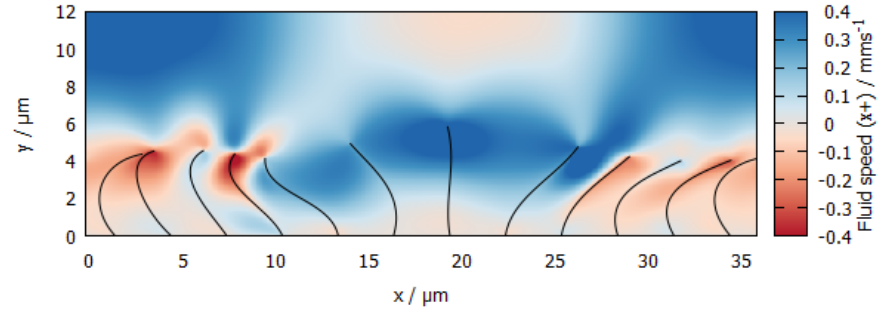

Figure 4.1: (a) A comparison of flow rates resulting from cilia beats with different phase step values: $\Delta\phi = \pi/12$ (red), $\Delta\phi = \pi/6$ (blue). cilium spacing is 3µm in both cases. (b) An example of the cilia profiles and fluid flow for $\Delta\phi = \pi/12$. Colour box represents fluid speed in the $x+$ direction. Figure shows a trimmed section of a larger fluid region. (c) An example of the cilia profiles and fluid flow for $\Delta\phi = \pi/6$. Colour box represents fluid speed in the $x+$ direction.

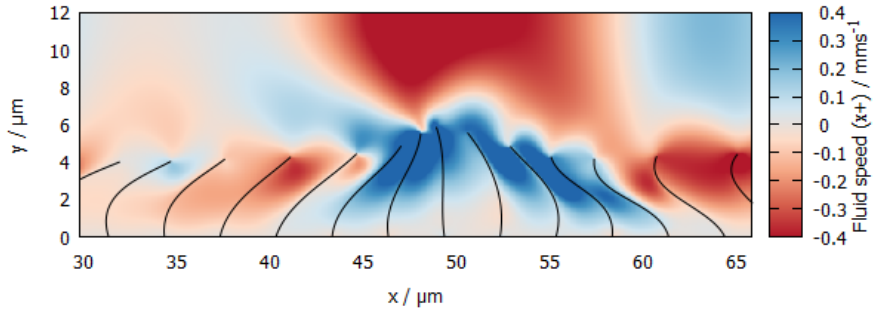

Figure 4.2: An example of the cilia clustering during their active stroke when $\Delta\phi = 23\pi/12$. Figure Shows a trimmed section of a larger fluid region. Colour bar represents fluid speed in the $x+$ direction.

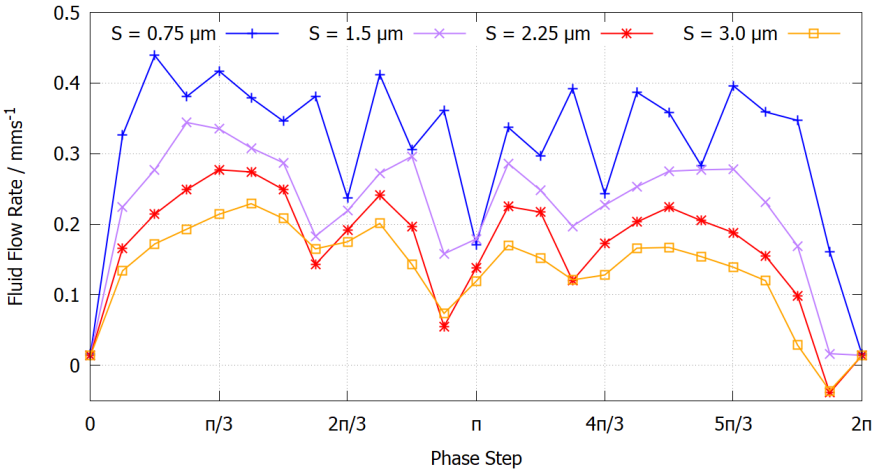

Figure 4.3: The observed relationship between phase step $\Delta\phi$ and fluid flow rate for a range of cilium spacing values.

and 3D simulations with slower fluid flow rates in all cases. This comparison is shown in figure 4.4b.

We have investigated the effect of a visco-elastic mucus layer on the observed behaviour by introducing a second fluid component with visco-elastic properties, and altering the cilia beat profile as described in section 3.2. The presence of the mucus layer altered the observed behaviour slightly but the distinctive features that we have identified were still present. It is clear from figure 4.5 that the relationship between phase step and fluid flow rates was largely unchanged by the presence of a visco-elastic mucus layer.

(a)

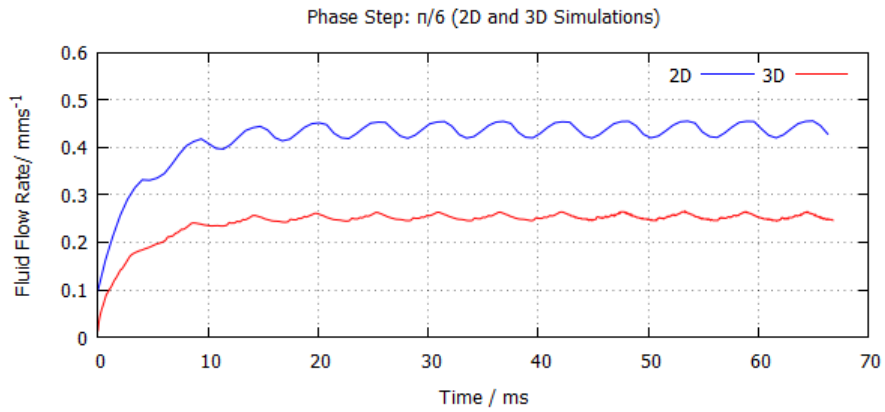

(b)

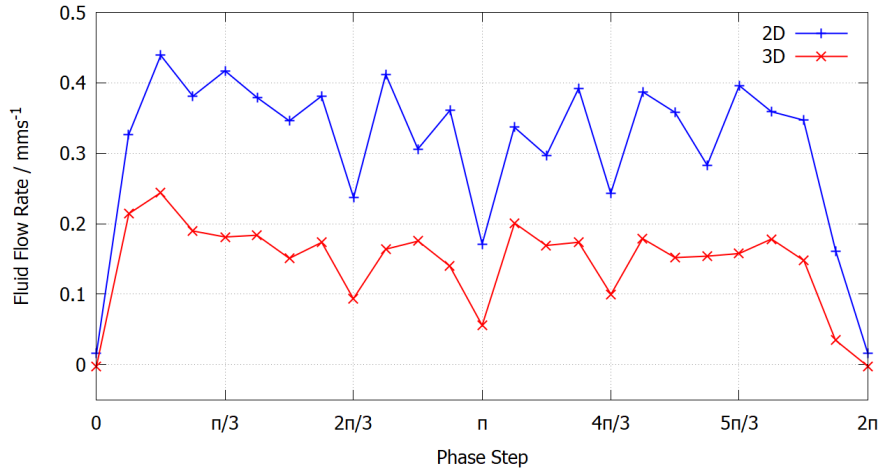

Figure 4.4: (a) A comparison of flow rates resulting from cilia beats in both a 2D (blue) and a 3D (red) fluid region. (c) A comparison of 2D and 3D simulation results for all phase step values with a cilium spacing of $0.75\mu m$.

4.2 Analytical Model

To quantify exactly how the clustering of cilia can affect fluid flow rate, we have formulated a simple analytical model of the cilium array. The analytical model is summarised by a single equation that we have used to calculate the area of fluid around the cilia that is free to flow. We refer to this quantity the free area, and use it as a numerical representation of the clustering of cilia in the array for a given cilium spacing and phase step.

4.2.1 Fluid Properties

Fluid properties were represented in our analytical model by the dissipation of fluid velocity over long distances. We have characterised this by simulating a large fluid region driven by a

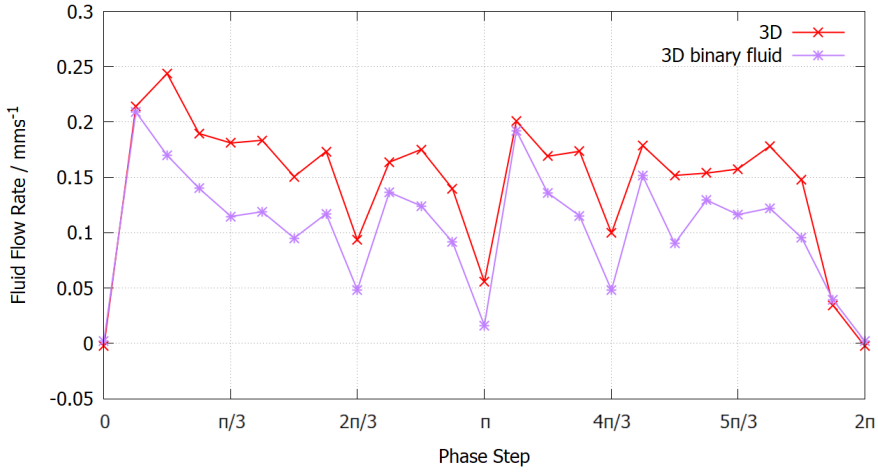

Figure 4.5: Comparing the relationship between phase step and flow rate for simulations with and without a visco-elastic mucus layer. Our results show similar behaviour in both cases with a cilium spacing of 0.75μm.

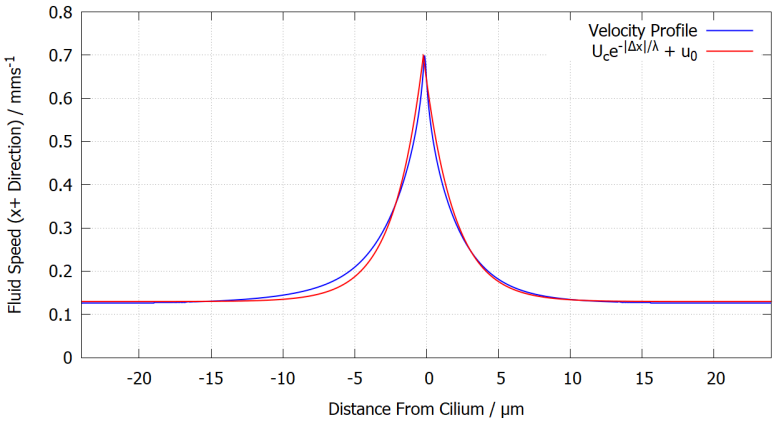

Figure 4.6: Observed fluid velocity as a function of distance from the cilium with a fitted exponential function for $\lambda = 2.44\mu m$

single cilium. By measuring the fluid velocity in the horizontal axis level with the cilium tip we observed that the dissipation of fluid velocity was well explained by an exponential function of the distance from the cilium as shown in figure 4.6. An investigation of this velocity profile and its relationship with the Reynolds number of our model is carried out in chapter 3. By fitting an exponential function to the velocity distribution

$$D_v = e^{-x/\lambda} \tag{4.1}$$

we found the characteristic length (λ) associated with the dissipation of fluid velocity representing the effective range of influence for a cilium in our analytical model.

4.2.2 Simplified Beat Profile

To determine the free area in the cilium array we developed a simplified form of the cilia beat profile to calculate the positions of all of the cilia in the array for a given time and phase step.

We assumed that each cilium remains straight throughout its beat cycle and moved through an active stroke where the cilium was fully extended moving through a 90° arc, and a recovery stroke where the cilium moved at half speed with a reduced length back to its initial position. Rather than shortening instantaneously, the cilium retracted and extended during the recovery stroke so that the beat profile was continuous at the transition between the two strokes as shown in figure 4.7.

The position of each cilium tip relative to its base was calculated as a function of the beat phase ($0 \le \phi \le 2\pi$). For the active stroke $\left(0 \le \phi < 2\pi/3\right)$ the position of the cilium tip was given by

$$x(\phi) = \frac{-\sqrt{2}L}{2}\cos\left(\frac{3}{2}\phi\right) \tag{4.2}$$

for the x coordinate, and

$$y(\phi) = \frac{L}{2}\left[1 + \frac{\sqrt{2}}{2} + \left(\frac{\sqrt{2}}{2} - 1\right)\cos\left(3\phi\right)\right] \tag{4.3}$$

for the y coordinate. Similarly for the recovery stroke $\left(2\pi/3 \le \phi < 2\pi\right)$ the position was given by

$$x(\phi) = \frac{2\sqrt{2}L}{5}\sin\left(\frac{3}{4}\phi\right) \tag{4.4}$$

and

$$y(\phi) = \frac{8+5\sqrt{2}}{20}L + \frac{8-5\sqrt{2}}{20}L\cos\left(\frac{3}{2}\phi\right). \tag{4.5}$$

This generated a continuous beat profile that was geometrically symmetrical but had a recovery stroke that was half the speed of the active stroke. A graphical representation of this beat cycle is shown in figure 4.7. We calculated the position of each cilium tip relative to a specific cilium (cilium 0) by taking the phase of each cilium to be

$$\phi_n = \phi_0 + n\Delta\phi \tag{4.6}$$

where ϕ_0 is the phase of cilium 0 and $\Delta\phi$ is the phase step. By substituting this relationship into equations 4.2-4.5 and accounting for the cilium spacing S we were able to calculate the position of each cilium tip relative to cilium 0 using

$$x_n(\phi_0, \Delta\phi) = nS + \frac{-\sqrt{2}L}{2}\cos\left[\frac{3}{2}(\phi_0 + n\Delta\phi)\right] \tag{4.7}$$

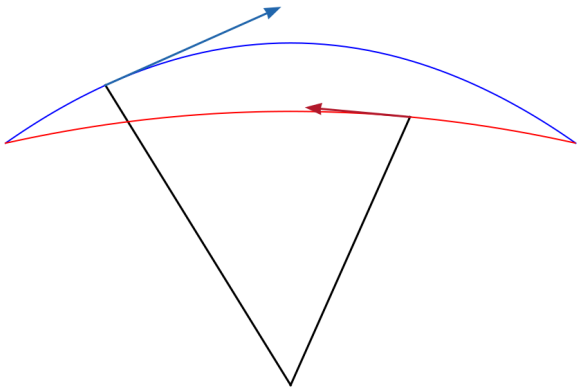

Figure 4.7: A graphical representation of the beat cycle of a single cilium in our analytical model. We have plotted a trace of the active stroke (blue) and the recovery stroke (red) for a full period of the phase angle ($0 \leq \phi \leq 2\pi$).

for the x coordinate, and

$$y_n(\phi_0, \Delta\phi) = \frac{L}{2}\left[1 + \frac{\sqrt{2}}{2} + \left(\frac{\sqrt{2}}{2} - 1\right)\cos\left[3(\phi_0 + n\Delta\phi)\right]\right] \tag{4.8}$$

for the y coordinate. Similarly for the recovery stroke $\left(2\pi/3 \leq (\phi_0 + n\Delta\phi) < 2\pi\right)$ the position was given by

$$x_n(\phi_0, \Delta\phi) = nS + \frac{2\sqrt{2}L}{5}\sin\left[\frac{3}{4}(\phi_0 + n\Delta\phi)\right] \tag{4.9}$$

and

$$y_n(\phi_0, \Delta\phi) = \frac{8 + 5\sqrt{2}}{20}L + \frac{8 - 5\sqrt{2}}{20}L\cos\left[\frac{3}{2}(\phi_0 + n\Delta\phi)\right]. \tag{4.10}$$

We have restricted our analytical model to the case where cilium 0 is half way through its active stroke ($\phi_0 = \pi/3$), because this was when a cilium would be moving fastest and driving fluid flow most effectively. By substituting this value for ϕ_0 in equations 4.7-4.10 we calculated the position of each cilium tip relative to the active cilium by

$$x_n(\Delta\phi) = nS + \frac{\sqrt{2}L}{2}\sin\left(\frac{3}{2}n\Delta\phi\right) \tag{4.11}$$

for the x coordinate, and

$$y_n(\Delta\phi) = \frac{L}{2}\left[1 + \frac{\sqrt{2}}{2} - \left(\frac{\sqrt{2}}{2} - 1\right)\cos\left(3n\Delta\phi\right)\right] \tag{4.12}$$

for the y coordinate. Similarly for the recovery stroke $\left(\pi/3 \leq \Delta\phi < 5\pi/3\right)$ the position was given by

$$x_n(\Delta\phi) = nS + \frac{2\sqrt{2}L}{5}\sin\left(\frac{\pi}{4} + \frac{3}{4}n\Delta\phi\right) \tag{4.13}$$

and

$$y_n(\Delta\phi) = \frac{8+5\sqrt{2}}{20}L - \frac{8-5\sqrt{2}}{20}L\sin\left(\frac{3}{2}n\Delta\phi\right). \tag{4.14}$$

Using these equations we were able to calculate the relative positions of all cilia in the array for a given phase step and cilium spacing.

4.2.3 Free Area Equation

We have defined free area as the area of fluid in the plane of the cilium beat that is free to flow when driven by the active stroke of a single cilium, taking into account the restriction of flow caused by the other cilia in the array. We calculated the effective area (E) of the active cilium by integrating the effective range (D_v) from equation 4.1 over the full range of x

$$E = 2H\int_0^\infty e^{-x/\lambda}dx \tag{4.15}$$

where H is the height of the fluid region, and a factor of two is included due to the symmetry of our analytical model. We note that the equation for the effective range was derived from the equation of the velocity profile (equation 3.1) in the case where the cilium is positioned at the origin. The resistance caused by the nth cilium in the array (R_n) was calculated as the area that was blocked by that cilium based on the position of the cilium base and the cilium tip

$$R_n = y_n\left(\frac{nS - x_n}{2} + \int_0^\infty e^{-x/\lambda}dx\right). \tag{4.16}$$

where x_n and y_n represent the position of the tip of cilium n, as defined by the simplified cilium beat profile that we have developed in section 4.2.2. We used the same definition for the effective range of a cilium as we described in section 4.2.1. The area calculated in equation 4.16 is represented graphically in figure 4.8. We calculated the free area (F) around the active cilium by subtracting the resistance caused by every other cilium in the array from the effective area of the active cilium

$$F = E - 2\sum_{n=1}^{\infty} R_n e^{-nS/\lambda} \tag{4.17}$$

where the resistance of each cilium was scaled exponentially with its distance from the active cilium using the same effective range as described in section 4.2.1. This gave us an equation for free area that was dependent on phase step and cilium spacing,

$$F = 2H\lambda - \sum_{n=1}^{\infty} y_n(nS - x_n + 2\lambda)e^{-nS/\lambda}. \tag{4.18}$$

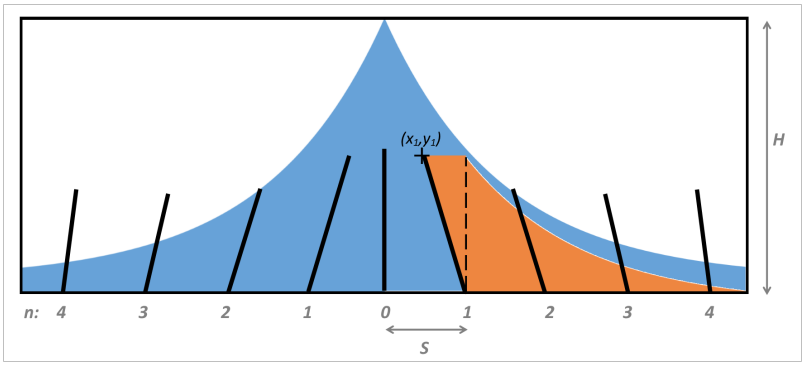

Figure 4.8: A graphical representation of the resistance caused by cilium 1 (Orange) as defined by equation 4.16, relative to the effective area of cilium 0 (blue) as defined by equation 4.15.

We note that this equation calculates the free area in the cilium array at a single point in time, when cilium 0 is mid way through its active stroke.

Using equation 4.18 combined with equations 4.11-4.12 we calculated the area of fluid that was theoretically free to flow for a given phase step and cilium spacing. This gave us a relationship that we could compare directly with the observed relationship between phase step, cilium spacing and fluid flow rate.

4.3 Results and Analysis

Our equation for free area represents a very specific relationship between free area and phase step, similar to the relationship that we have observed between fluid flow rate and phase step. By comparing the two as in figure 4.9a we can see that there is a direct correlation between free area and flow rate.

We observed that the correlation between flow rate and free area holds for different cilium spacings, as shown in figure 4.9d. By calculating the Pearson's correlation coefficient (r) for each different cilium spacing using

$$r = \frac{N\sum XY - (\sum X \sum Y)}{\sqrt{[N\sum x^2 - (\sum x)^2][N\sum y^2 - (\sum y)^2]}} \tag{4.19}$$

we have quantified how strong the correlation between our analytical model and simulation results is, and whether this correlation is dependant on cilium spacing.

Cilium Spacing / μm	Pearson's Correlation Coefficient
0.75	0.860
1.5	0.877
2.25	0.838
3.0	0.870

Table 4.1: Pearson's correlation coefficient for different cilium spacings

(a)

(b)

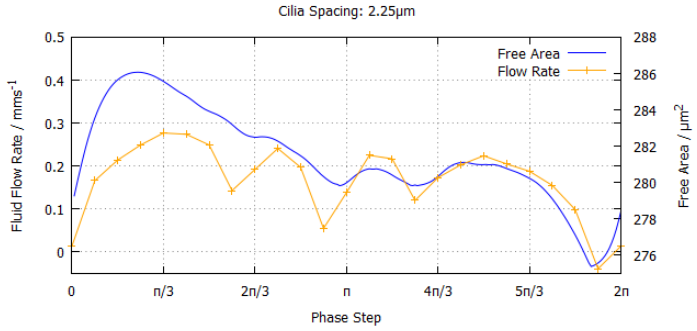

(c)

(d)

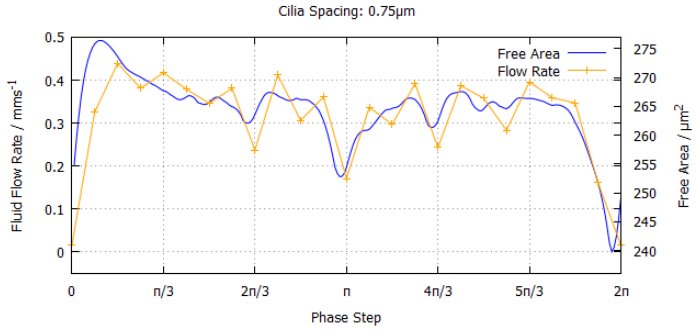

Figure 4.9: A direct comparison of the free area calculated from our analytical model and the fluid flow rate generated by our simulations showing a strong correlation between the two for a range of cilium spacing values (a) 3.0µm (b) 2.25µm (c) 1.5µm (d) 0.75µm

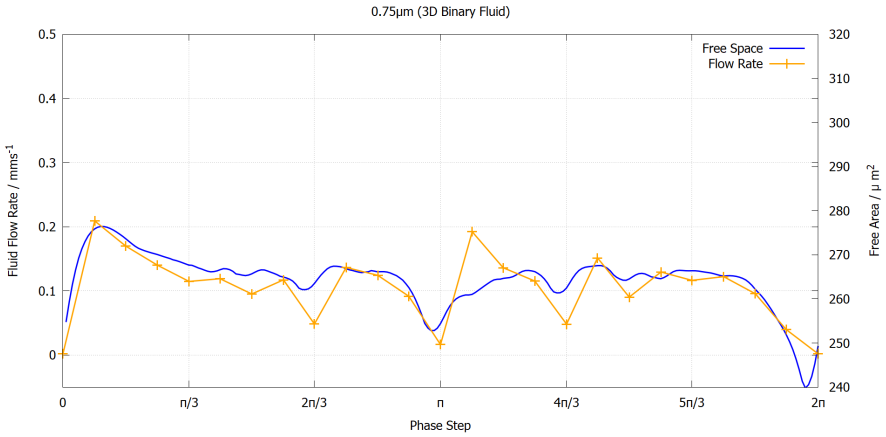

Figure 4.10: Comparing free area and flow rate with results from simulations with a visco-elastic mucus layer present shows the same correlation as observed without a visco-elastic layer.

The results in Table 4.1 show that there is a consistent positive correlation between our analytical model and simulation results. This confirms that the correlation between free area and flow rate was not only strong but also independent of cilium spacing. This implies that the variation of flow rate in our numerical model is largely due to the geometric properties of the cilium array, since our free area model does not factor in any complex hydrodynamic effects such as capillary force. We also observed that the optimal metachronal wavelength given by our simulations and our analytical model ($\lambda_M \approx 9\mu$m) was within the range of metachronal wavelengths observed in vitro [15].

We have seen in section 4.1 that the presence of the mucus layer has a minimal effect on the observed relationship between phase step and fluid flow rate. Although results in section 3.2 show that the velocity profile in a binary fluid is somewhat different to the one used in our analytical model. Despite the change in the velocity profile, the correlation that we observed between free area and flow rate holds true for the case where visco-elastic mucus is present in the simulation. These results are shown in figure 4.10.

From the results in figures 4.9 and 4.10 we can see that while there is a clear link between free area and flow rate, the data also implies that there is an amount of free area that does not contribute to the fluid flow. This is because only fluid that is above the cilium array flows consistently, and the fluid that the surrounds the cilium array will flow back and forth as the cilia beat. It is clear from our analytical results that the free area in the lower fluid region is vital for effective fluid flow although the fluid in this region does not necessarily contribute to the net fluid flow.

Our simulation results generally showed that the lowest values for fluid flow rate correspond with synchronised beating. However there were some cases where these minima were offset from synchrony and the lowest values of fluid flow rate corresponded with symplectic metachrony. A good example of this occurred when the cilium spacing was 2.25µm as in figure 4.9b. Similar

behaviour has been observed by Ding et al. [11]. We propose that this behaviour was due to the minimal free area associated with symplectic metachrony which reduced the effectiveness of the active stroke to the point where the recovery stroke was actually more effective at driving fluid flow, as predicted by our analytical model.

4.4 Summary

We have conducted a number of numerical simulations in order to identify how the metachronal wavelength of a beating cilium array affects the rate of fluid flow. Based on the results of these simulations we have derived a simple analytical model of the cilium array to determine the free area of fluid that is available to each cilium as it beats, and how this value depends on the phase step. By comparing our analytical model with our simulation results we have determined that there is a strong correlation between free area and fluid flow rate, which supports the validity of our analytical model.

Both our analytical and simulation results indicated that an antiplectic metachronal wave ($\Delta\phi < \pi$) was more effective at generating fluid flow than a symplectic wave ($\Delta\phi > \pi$), which agrees with other simulations [6, 27]. Our simulation results also showed that symplectic metachrony could be even less effective at generating fluid flow than synchronised beating, in agreement with the work of Ding et al. [11]. Using our analytical model we were able to attribute this behaviour to there being a greater amount of free area during the recovery stroke than the active stroke, which meant that the recovery stroke was able to produce fluid flow in the opposite direction.

5

APPLICATIONS

In this chapter we apply our model to help elucidate the physics associated with the two phenomina of metachronal beating and de-ciliated regions.

We present the results of a study building upon the work of Jayathilake et al. [24] which found that the introduction of metachronal beating to 3D array of cilia dramatically increases the fluid flow rate. We show that our initial results are consistent with these observations, and additionally we show that this behaviour is sensitive to changes in the cilium spacing. We also explore how this behaviour is affected by the presence of a visco-elastic mucus layer.

We then discuss the results from our study on the effect of de-ciliated regions on fluid flow rate. In this study we define the four different cases for de-ciliated regions that represent different densities and arrangements of cells to see how both factors affect fluid flow. We directly compare the flow rates generated in each case and give insights into observed changes to flow rate caused by different layouts of ciliated cells.

5.1 Metachronal Beating

We have used our numerical model to gain further insight into an important observation from Jayathilake et al. [24] to explore how the effect of introducing metachrony to a cilium array is altered by cilium spacing and the presence of a visco-elastic mucus layer. Jayathilake et al. created a model of cilia driven fluid flow using the staggered grid immersed boundary method. They used this model to simulate a single component fluid driven by an array of 72 cilia generating flow with three variations in metachrony [24]:

A. Synchronised beating

B. Antiplectic metachrony

C. Antiplectic and diaplectic metachrony

A graphical representation of these three states is shown in figure 1.4. These simulations were performed with a cilium spacing of 3μm (half of one cilium length), and periodic boundaries

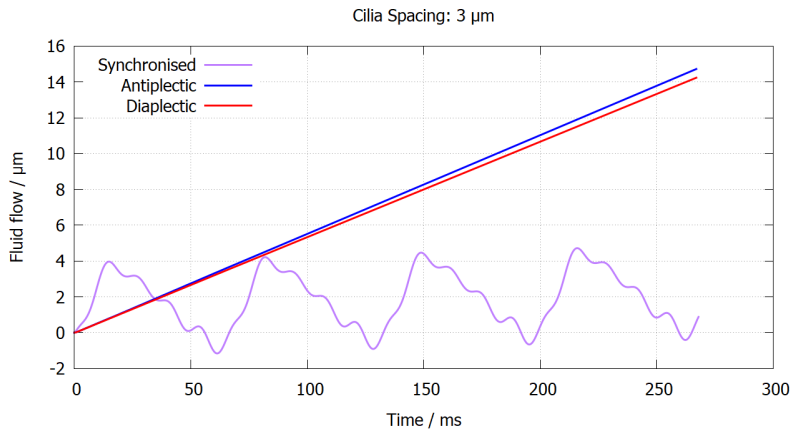

Figure 5.1: Simulation results showing the effects of introducing antiplectic and diaplectic metachrony to an array of beating cilia. The value plotted on the y axis corresponds to the fluid flow as defined by equation 2.29. These results are consistent with the observations of Jayathilake et al. [24]

were used to ensure consistent fluid flow through the cilium array. The cilia beat frequency for these simulations was 10Hz. The results from these simulations showed that the introduction of antiplectic metachrony caused a significant increase in the fluid flow rate and the consistency of the fluid flow, as seen in figure 1.5. In addition to this the introduction of diaplectic metachrony caused a further increase in flow rate [24]. A more detailed description of these results is given in Section 1.1.2.

The cilia beat frequency that we used was 15Hz and our cilia beat pattern was strictly planar, as described in section 2.2. The layout of the cilium array used in our simulations was a square with the cilia arragned in straight rows and columns as shown in figure 5.2. For these simulations we used a 12×12 array of cilia (144 cilia in total) to generate fluid flow. Initial results from these simulations showed a significant increase in fluid flow for cilia beating in an antiplectic metachronal wave relative to cilia beating in synchrony, as shown in figure 5.1. This result is as expected when we consider that the fluid dynamics of water at this scale are largely dominated by viscous effects, so there is no inertia to maintain fluid flow between active strokes. Beating in a metachronal wave means that there is a wavefront of active cilia that constantly moves through the fluid region so that the fluid is being driven by this active region at any given time. When we introduced diaplectic metachrony into our simulations we saw that the fluid flow rate decreased slightly. This is likely due to the lack of extra planar cilia beating in our model, meaning that there is no advantage to diaplectic metachrony over antiplectic metachrony in this case. Examples of our cilium array beating in antiplectic and diaplectic metachrony are shown in figure 5.2.

We have carried out simulations on the effect of cilium spacing on the observed behaviour caused by metachronal waves in the cilium array. Our results in figure 5.3a show that reducing the cilium spacing slightly decreased the flow rate for the synchronised case, but it also seemed to

(a)

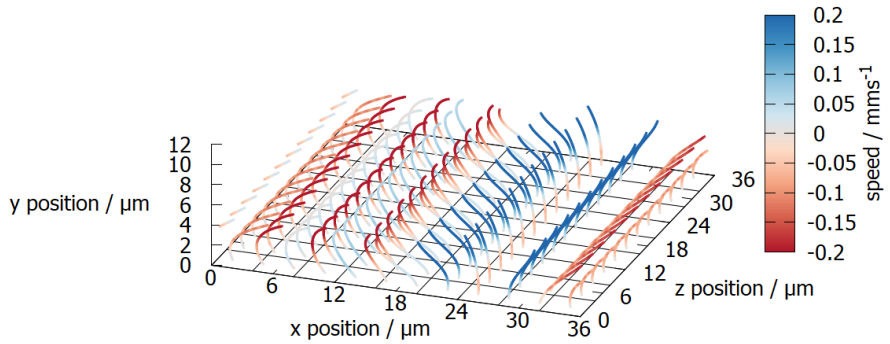

(b)

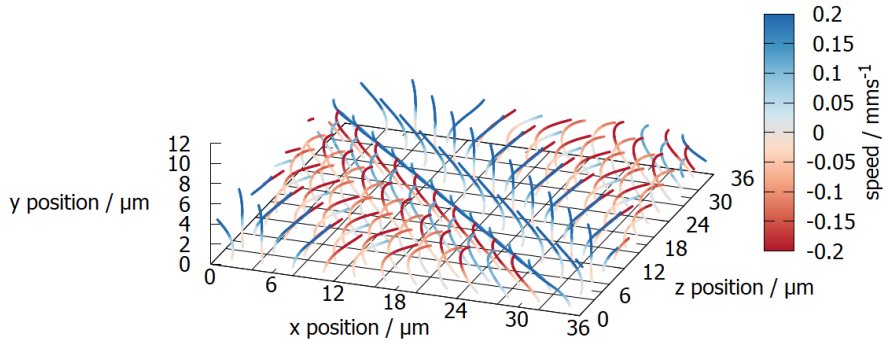

Figure 5.2: (a) An example of a 12×12 array of cilia beating with an antiplectic metachronal wave. (b) The same array of cilia beating with both an antiplectic and diaplectic wave.

magnify the effect of metachrony on the fluid flow rate. We observe that the increase in flow rate due to the metachronal wave was significantly larger when the cilium spacing was smaller. This suggests that metachrony is more effective at accelerating fluid flow when the cilium spacing is smaller, which is supported by the observation by Chateau et al [6] that the influence of metachrony is reduced for large cilium spacings. We note that our simulation data also shows a small decrease in flow rate when a diaplectic metachronal wave is present for smaller cilium spacings.

We have run further simulations with a visco-elastic mucus layer present in the fluid to discern what effect this has on the observed behaviour. The mucus layer begins at a height of 5.4µm so that cilia only interact with the mucus during their active stroke. The beat profile used in our model was altered to account for the presence of the mucus layer so that each cilium

(a)

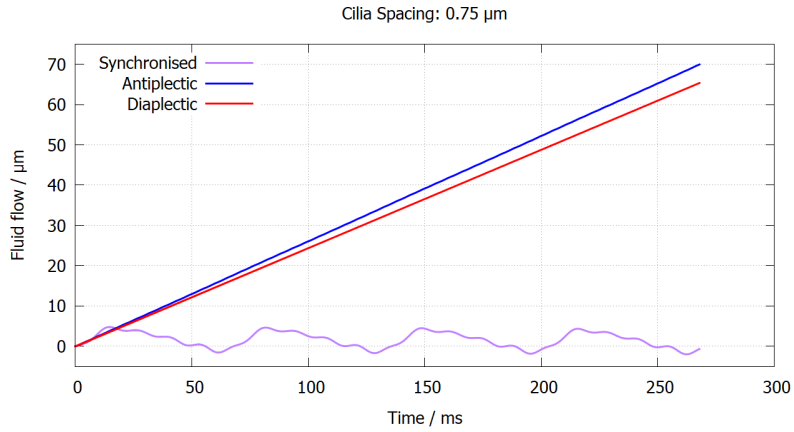

(b)

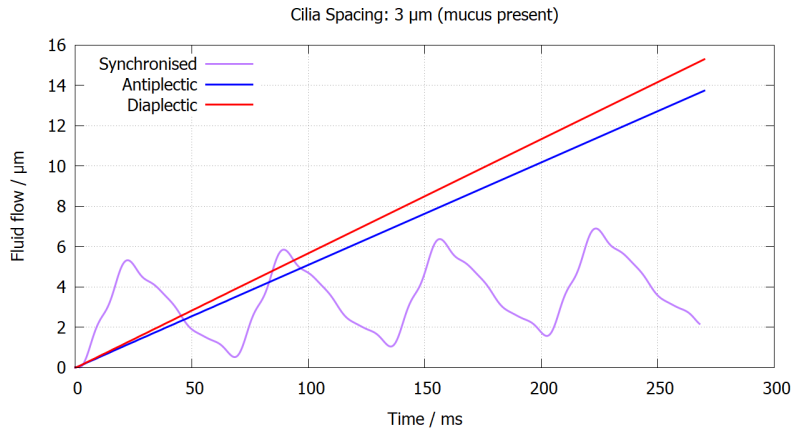

Figure 5.3: Results highlighting the effect of different metachronal wave configurations when a) the cilium spacing is reduced to 0.75µm and b) A visco-elastic mucus layer is present in the fluid. The value plotted on the y axis corresponds to the fluid flow as defined by equation 2.29.

moves more slowly when it enters the mucus [14]. We observed from our results in figure 5.3b that the presence of the mucus layer resulted in faster fluid flow for the synchronised case due to the cilia only interacting with the mucus layer during the active stroke. The introduction of an antiplectic metachronal wave caused an increase in flow rate similar to what we observed without the mucus layer, but in this case the diaplectic wave caused a further increase in the flow rate. Since the beat profile used in our model is still planar, this change in behaviour is likely due to the visco-elastic properties of the mucus layer.

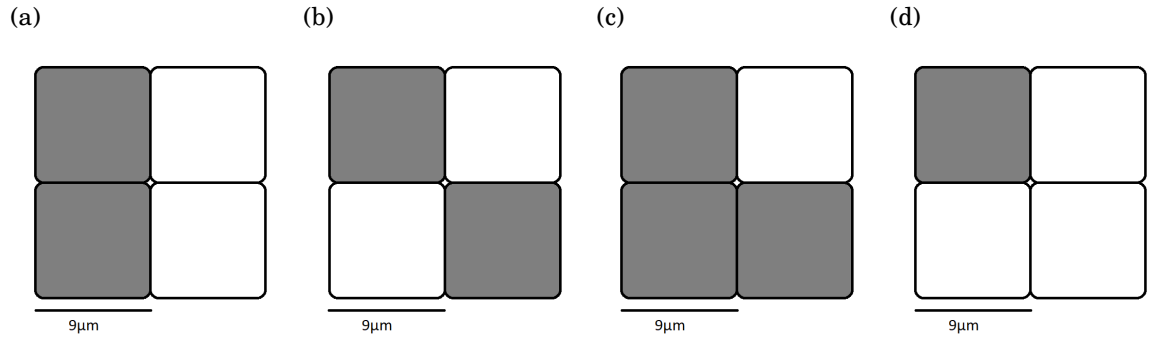

Figure 5.4: A graphical representation of the four states used to investigate the effects of de-ciliated regions on fluid flow. Cases are shown in a top down view of the epithelial cells where shaded cells are ciliated and white cells are de-ciliated. (a) Case $\mathscr{A}$: 50% de-ciliated cells in straight rows (b) Case $\mathscr{B}$: 50% de-ciliated cells arranged in a grid (c) Case $\mathscr{C}$: 25% de-ciliated cells separated by ciliated regions (d) Case $\mathscr{D}$: 75% de-ciliated cells with isolated ciliated cells.

5.2 Deciliated Regions

As mentioned in section 1.2.3, the epithelium is not entirely made up of ciliated cells [2]. The presence of goblet cells and other non-ciliated cells on the epithelium means that there are regions without cilia that therefore do not contribute to muco-ciliary clearance. It has also been found that certain disease states such as Asthma and COPD can cause goblet cell hyperplasia and squamous metaplasia that would result in large regions of the epithelium being de-ciliated [1, 42].

We used our model to investigate how cilia driven fluid flow was affected by the presence of these de-ciliated regions and whether the density and positioning of the de-ciliated regions altered the resulting fluid flow. To do this, we defined 4 different test cases that represented a variety of densities and layouts for de-ciliated regions. A graphical representation of each case is shown in figure 5.4. The use of periodic boundary conditions in our model means that the regions shown are repeated in all directions to form a consistent pattern of ciliated and de-ciliated cells. Each cell was represented in our simulations by a 9×9μm square, and the ciliated cells contained a uniform array of 12×12 cilia which beat in a coordinated pattern as shown in figure 5.2b. For this investigation we used a cilium spacing of 0.75μm and a phase step of $\pi/6$ so that we could represent the in vivo system as closely as possible. Using these parameters also means that a cell measuring 9μm contains a single metachronal wavelength in both the x and z directions.

Case $\mathscr{A}$ represents a situation where 50% of epithelial cells are de-ciliated and the de-ciliated cells are adjacent to one another forming rows of ciliated and de-ciliated cells as shown in figure 5.4a. Case $\mathscr{B}$ also represents a situation where 50% of cells are de-ciliated but in this case the de-ciliated cells are arranged in a grid such that the cells alternate from ciliated to de-ciliated in all cardinal directions as shown in figure 5.4b. In case $\mathscr{C}$ only 25% of cells are de-ciliated and each of these cells is surrounded by a region of ciliated cells as shown in figure 5.5c. In case $\mathscr{D}$

(a) (b)

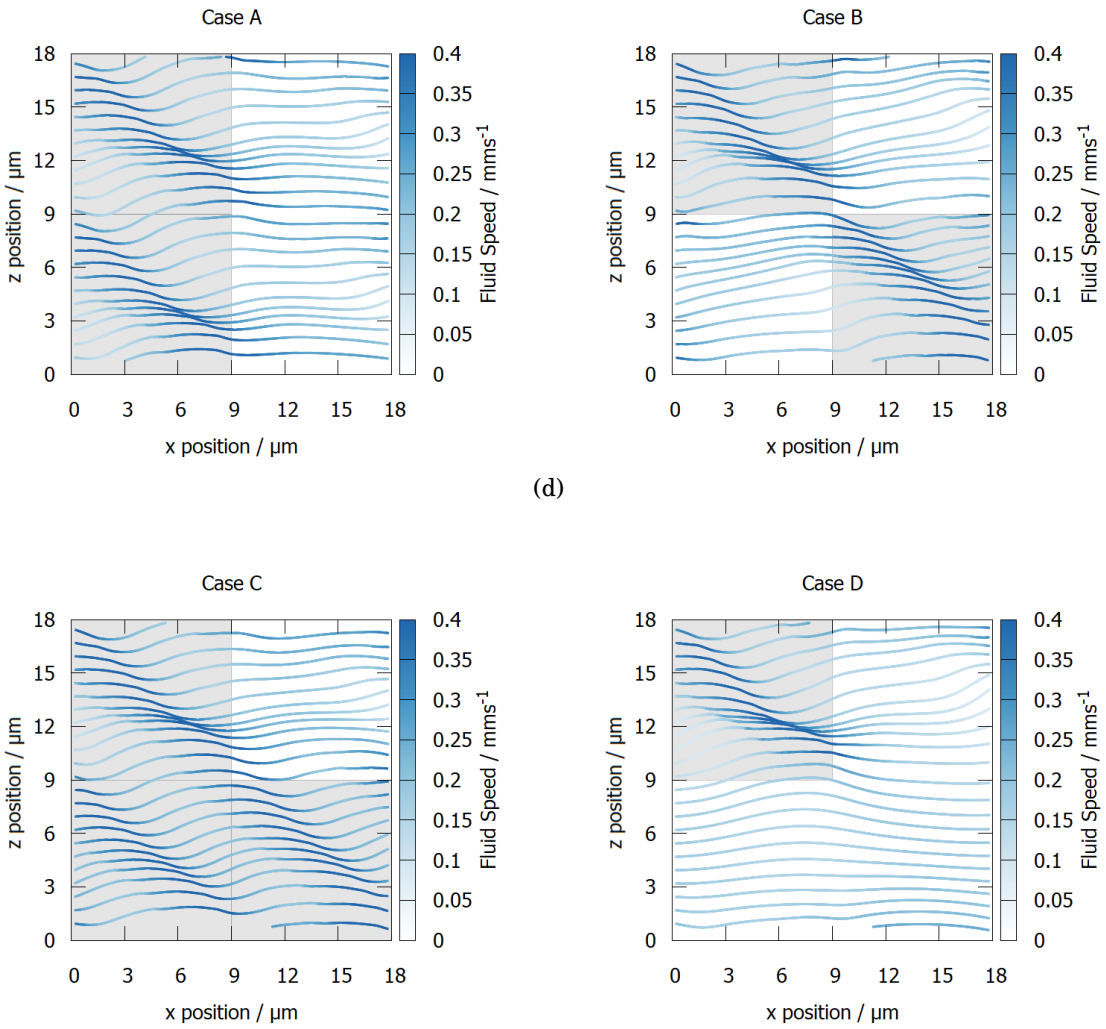

(c) (d)

Figure 5.5: A top down view of fluid flow in the mucus layer for each case of de-ciliated regions. Streamlines shown represent fluid flow at a height of 6µm. Ciliated cells in each case are indicated by shaded regions

75% of cells are de-ciliated and ciliated cells are completely isolated from each other as shown in figure 5.5d. In the results that follow we also refer to the case where there is no de-ciliated region present as case $\mathcal{I}$ for ease of comparison.

Plotting the fluid flow in the mucus layer, as in figure 5.5, shows that although the fluid flow is positive through out the fluid region the acceleration of fluid due to the active stroke is clearly visible. This allows us to directly observe how the fluid flow is altered by the layout of ciliated cells.

Using the cases described here we have been able to investigate how the fluid flow rate varies

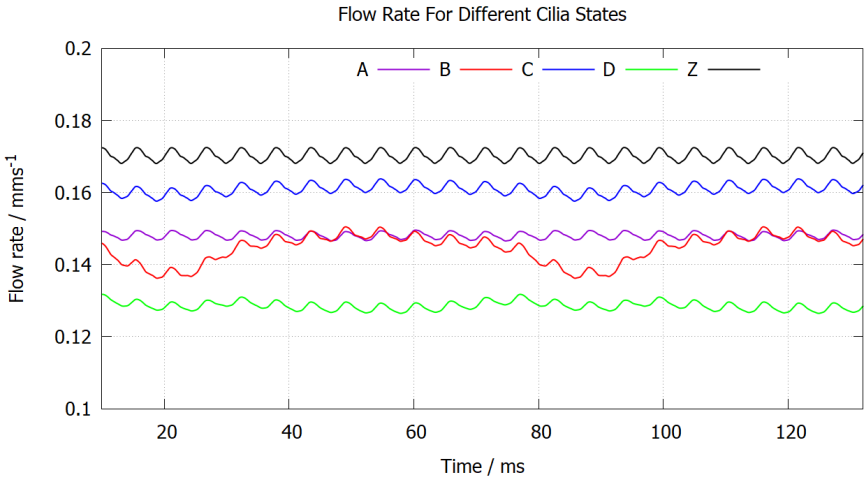

Figure 5.6: flow rates generated by each case that we have defined for de-ciliated regions. The figure shows a moving average of the simulation data to reduce noise and make the differences between the states clearer. We also negate results from the first 10 ms of the simulation when the flow rate is not yet steady.

Table 5.1: Flow rates for each case of de-ciliated regions

Case	Avg. Flow Rate / $\mathrm{mm\,s^{-1}}$	% of Cells Ciliated	% of Max Flow Rate
$\mathscr{A}$	0.148	50%	87%
$\mathscr{B}$	0.144	50%	85%
$\mathscr{C}$	0.161	75%	95%
$\mathscr{D}$	0.128	25%	75%
$\mathscr{Z}$	0.170	100%	100%

with both the density of de-ciliated regions and the layout of these regions. A direct comparison of the flow rates produced by simulating each state are shown in figure 5.6. We note that the recorded flow rates oscillate over time due to the delay between active strokes of each cilium, and that there is a large overlap in the recorded flow rate data for the five cases. Because of this we have plotted a moving average of the flow rate to reduce noise in the presented data. This also highlights the regular fluctuations of the flow rates over time.

We can see from the results in table 5.1 that the flow rate is clearly related to number of ciliated cells in the fluid region, but by comparing the flow rates with that of case $\mathscr{Z}$ it is also clear that this relationship is non-linear. By comparing the flow rates for the two 50% de-ciliated cases we can also see that the relationship is dependant on the layout of the ciliated cells.

The fluctuations in flow rate that we observed for case $\mathscr{B}$ were caused by the specific layout of ciliated cells causing a change in the coordination between those cells. The key difference between case $\mathscr{A}$ and case $\mathscr{B}$ is the distance between the cilia that are beating in their active stroke. We can see from figure 5.2 that due to the metachronal beating of the cilium array the active cilia form a wave front that spans across the parallel rows of cilia. Specifically in the case

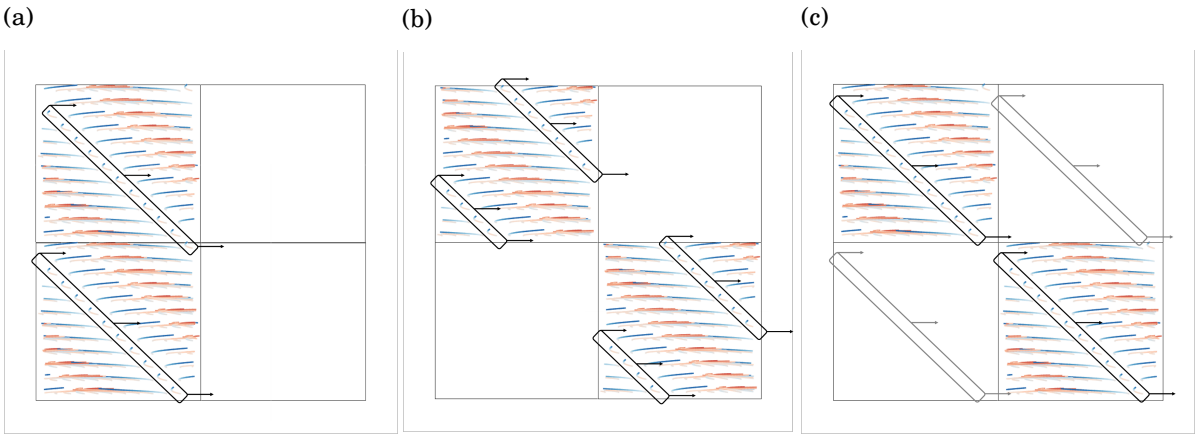

Figure 5.7: A graphical representation of ciliated cells from a top down view, showing the combination of antiplectic and diaplectic metachrony present in the cilia array. Wave fronts of cilia in their active stroke are highlighted with black bars. (a) In case $\mathscr{A}$ the active wave front is equally spaced at all times (b) Case $\mathscr{B}$ has the same minimum distance in most cases. (c) At specific times the minimum distance between wave fronts doubles due to the layout of the ciliated cells. We have shown the position of a "missing" wave front with a grey bar.

of antiplectic and diaplectic metachrony, this wave front spans diagonally across the ciliated cell. This wave front creates a fast flowing region in the fluid that surrounds it, as shown in figure 5.5. The distance between these wave fronts parallel to the rows of cilia would simply be 1 metachronal wavelength (9μm in this case), depending on whether the adjacent cells in that direction are ciliated. Measuring normal to the wave front gives a distance of $1/\sqrt{2}$ metachronal wavelengths ($9/\sqrt{2}$μm in this case), and this distance depends on whether the adjacent cells in any direction are ciliated. This is also the minimum distance between wave fronts.

Most of the time the minimum distance between wave fronts in case $\mathscr{B}$ is $9/\sqrt{2}$μm, the same as in case $\mathscr{A}$ as shown in figures 5.7a and 5.7b. At specific times in our simulations the minimum distance between wave fronts in case $\mathscr{B}$ increases to $18/\sqrt{2}$μm, as shown in figure 5.7c. This was a direct result of the layout of the ciliated cells, since there would also have been a wave front at the point where the two cells meet (highlighted in grey). Due to the layout of ciliated cells this wave front was missing and hence the distance between the remaining wave fronts was twice as large as in case $\mathscr{A}$ for the same time.

These results implied that in certain cases the presence of de-ciliated regions can disrupt the coordination of metachronal waves. In this case we have seen that when the distance between active cilia is increased without altering the metachronal wavelength the coordination between metachronal waves is essentially broken. Without this coordination each wave drives the fluid independently, resulting in a slower fluid flow rate. This is typified by the way that the flow rate in case $\mathscr{B}$ fluctuates between the flow rates of case $\mathscr{A}$ and case $\mathscr{D}$ depending on the spacing of the active wave fronts.

5.3 Summary

In this chapter we have built upon the results of Jayathilake et al. [24] indicating that introducing antiplectic metachrony into an array of beating cilia causes a significant increase to the resulting fluid flow rate. We expanded on the previous work by investigating the effects of antiplectic and diaplectic metachrony for an array of cilia with a smaller cilium spacing ($S = 0.75\mu m$) which caused a greater increase in flow rate when metachrony was introduced. This result is consistent with previous observations that the coordination of beating cilia depends on the distances between them [6]. We have also simulated this behaviour in the presence of a visco-elastic mucus layer. We observed the same increase in fluid flow rate when antiplectic metachrony was introduced, and we also observed a slight increase in fluid flow rate when diaplectic metachrony was introduced. We reasoned that the change in behaviour was most likely caused by the visco-elastic properties of the mucus layer.

We have also investigated the effects of de-ciliated regions on fluid flow by simulating fluid driven by ciliated cells that are separated by de-ciliated regions in four different configurations. The results from this investigation showed that the arrangement of ciliated cells played a role in the coordination of cilia beating to drive fluid flow. By inspecting the wave fronts of active cilia in the case when the two ciliated cells were adjacent to one another and when they were offset diagonally from one another, we were able to discern that the distance between these active wave fronts was larger at certain times in the second case. The times when this distance was larger coincided with a reduction in fluid flow rate. This lead us to the conclusion that the distance between the active wave fronts was an important part of the coordinated beating for cilia driven flow. In the case that the distance between the wave fronts is too large there is no interaction between the metachronal waves and each one drives the fluid independently, resulting in slower fluid flow.

6

DISCUSSION

In this chapter we first present a summary of the results from each investigation that we have carried out as part of this project and discuss some of their implications. We then go on to discuss some ideas for work that could be done in the future based on our results. This work could either take the form of verifying our results experimentally, or developing our numerical model to conduct simulations of more complex behaviours associated with mucus rheology. Finally we present the conclusions that we have drawn from our results.

6.1 Summary of Results

We first investigated the fluid flow behaviours associated with an isolated cilium by looking at the instantaneous fluid velocity profile during the active stroke of the cilium. We found that in the x direction the fluid velocity decayed exponentially with distance from the cilium, and that the velocity profile could be represented by an exponential function of distance with the characteristic length λ. We used λ to quantify changes in the velocity profile for different Reynolds numbers, and observed that for low Re the characteristic length converged to $\lambda = 2.44\mu$m. For high Re the exponential fit became less valid due to the presence of rotational flow in the fluid. We also found that the velocity profile in the y direction varied with Re in a way that was consistent with the increase of viscosity, as observed in other simulation results from the literature [22, 45]. We showed how these velocity profiles were altered by the presence of a visco-elastic mucus layer, meaning that the exponential fit that we used before was no longer valid. We also showed an example of shear banding that occurred between the two fluid layers during the recovery stroke.

We then looked at the effect of metachronal wavelength on fluid flow rate by varying the phase step between adjacent cilia. We observed the relationship between phase step and flow rate, and that this relationship was sensitive to changes in the cilium spacing. Results from these simulations implied a link between the clustering of cilia and the effectiveness of the active stroke. Based on these results we formulated an analytical model to quantify the clustering of cilia by calculating the area of fluid that was free to flow based on the cilium spacing, the phase step, and the characteristic length of the velocity profile. The free area calculated by our analytical model

showed a very strong correlation with the fluid flow rate, and the correlation was independent of cilium spacing. This correlation was also largely unaffected by the presence of a visco-elastic mucus layer. These results implied that the variation of fluid flow rate with phase step that we have observed is largely due to changes in the geometry of the cilium array.

As an application of our numerical model, we have built upon the work of Jayathilake et al. [24] by comparing fluid flow generated by synchronised and metachronal beating, and how this behaviour is affected by cilium spacing. We observed the same significant increase in fluid flow for cilia beating in an antiplectic metachronal wave when compared with synchronised cilia. In our simulations the inclusion of diaplectic metachrony caused a slight decrease in flow rate, as opposed to the increase that was observed by Jayathilake et al. We attributed this to the cilium beat profile that we used being planar rather than 3D, meaning that there was no benefit to diaplectic metachrony when compared with antiplectic metachrony. We went on to repeat these simulations for a smaller cilium spacing which magnified the effect of antiplectic metachrony, causing a greater increase in fluid flow than for the larger cilium spacing. These results supported the idea that coordinated beating has a greater affect when cilia are closer together. We also repeated these simulations with the inclusion of a visco-elastic mucus layer and observed that this altered the effect of diaplectic metachrony, causing a slight increase in fluid flow rather than the decrease that we observed for the single fluid case. We discerned that this change was most likely due to the visco-elastic properties of the mucus.

We also investigated the affect of de-ciliated regions on fluid flow by simulating fully ciliated cells separated by de-ciliated regions in four different arrangements. Results from these simulations indicated that there was a non-linear relationship between the number of ciliated cells in the fluid region and the fluid flow rate, and that the arrangement of the ciliated cells had an affect on fluid flow. The case where ciliated cells were arranged diagonally showed a periodic drop in fluid flow rate when compared with the case where the same number of ciliated cells were arranged in rows. We observed that the drop in flow rate was associated with an increase in the distance between wave fronts of active cilia on the cells, which in turn was caused by a missing wave front due to the arrangement of ciliated cells. We concluded that the greater distance between active wave fronts was preventing the ciliated cells from coordinating to drive fluid flow, which resulted in fluid flows comparable to those observed for a ciliated cell driving fluid flow in isolation.

6.2 Further Work

Generally the next stage for work like this would be to verify the results of our simulations with experimental work. However, for most of the results that we have discussed this is virtually impossible with cilia in vitro. Recreating the simulations that we have carried out would require controlling the cilia to a degree that is not currently possible with naturally occurring cilia. There

has been a lot of work in recent years towards the creation of artificial cilia that can be controlled by a magnetic field or some similar method [20]. Artificial cilia could be used to reproduce some of our results experimentally by, for example, imposing different metachronal wavelengths onto the cilia array and observing the resultant changes to fluid flow. Some of our results could even be used to predict the optimal parameters for artificial cilia to be used for practical applications.

Our model of a binary fluid with visco-elastic properties has proven effective for simulating fluid flow for different cases of cilia driven flow, but modelling the two fluid components as immiscible fluids has its limitations. The introduction of a more comprehensive model for mucus that includes the specific properties of a polymer gel could allow us to simulate some of the more complex behaviours of mucus such as mucus layer hydration and mucin tethering. A theoretical study of these processes could give us more insight into the symptoms of diseases like COPD and Asthma.

A more comprehensive model of mucus rheology combined with our model for cilia driven fluid flow could also be used to investigate the behaviour of particles within the mucus layer. Results from clinical studies in the literature indicate that smaller particles are able to reach the epithelium more easily [49], and that nanoparticles could be used to deliver medication directly to the epithelium for treatment of asthma and other diseases [3, 21]. With a robust model of mucus as a polymer gel we should be able to accurately simulate the diffusion of nanoparticles through the mucus layer to the epithelium to give a clear picture of exactly how the size and shape of the particles affects this process. We could also look at the effect of dehydration of the mucus layer, and how that might impede the diffusion of nanoparticles to the epithelium. It may even be possible to simulate the observed effect that the presence of nanoparticles has on the secretion and hydration of mucins [8, 9].

6.3 Conclusion

The results from our investigation into the effect of metachronal wavelength on fluid flow rate show that the clustering of cilia during the beat cycle has a significant effect on the effectiveness of cilia driven flow. We were also able to quantify this behaviour using an analytical model of the cilium array. We can conclude from these results that the geometry of the cilium array is the main contributor to the changes in fluid flow that we observed, as opposed to hydrodynamic effects such as capillary forces.

Results from all of our investigations have lead us to the same conclusion that coordinated cilia beating is only effective for driving fluid flow if cilia are in close proximity to one another. We saw this expressed as the characteristic length associated with the fluid velocity profile due to a single beating cilium, which in turn played a role in our analytical model to calculate the free area in the cilium array. We also observed that the increase in flow rate due to metachronal beating was significantly greater when the cilium spacing was reduced, which again implies

that the effect of coordinated beating is greater for more densely packed cilia. We observed a similar effect when investigating the effect of de-ciliated regions on fluid flow. We found that if the distance between regions of active cilia was above a certain threshold then the coordination of cilia beating between ciliated cells was no longer effective, and the ciliated cells would drive fluid flow as if they were in isolation. This behaviour was expressed by a periodic drop in the fluid flow rate when the ciliated cells were arranged diagonally.

The common theme that is evident in all of our results is that each behaviour that we have encountered can be attributed in some way to the geometry of the cilium array and the spaces between beating cilia.

BIBLIOGRAPHY

[1] *ABC of COPD*, ABC series (Malden, Mass.), Wiley Blackwell : BMJ Books, Hoboken, New Jersey, third edition. ed., 2017.

[2] L. H. ABDULLAH AND C. W. DAVIS, *Regulation of airway goblet cell mucin secretion by tyrosine phosphorylation signaling pathways*, American Journal of Physiology - Lung Cellular and Molecular Physiology, 293 (2007), pp. L591–L599.

[3] S. AZARMI, W. H. ROA, AND R. LOEBENBERG, *Targeted delivery of nanoparticles for the treatment of lung diseases*, ADVANCED DRUG DELIVERY REVIEWS, 60 (2008), pp. 863–875.

[4] L. R. BONSER, L. ZLOCK, W. FINKBEINER, AND D. J. ERLE, *Epithelial tethering of MUC5AC-rich mucus impairs mucociliary transport in asthma*, JOURNAL OF CLINICAL INVESTIGATION, 126 (2016), pp. 2367–2371.

[5] B. BUTTON, L.-H. CAI, C. EHRE, M. KESIMER, D. B. HILL, J. K. SHEEHAN, R. C. BOUCHER, AND M. RUBINSTEIN, *A Periciliary Brush Promotes the Lung Health by Separating the Mucus Layer from Airway Epithelia*, SCIENCE, 337 (2012), pp. 937–941.

[6] S. CHATEAU, J. FAVIER, U. D'ORTONA, AND S. PONCET, *Transport efficiency of metachronal waves in 3D cilium arrays immersed in a two-phase flow*, JOURNAL OF FLUID MECHANICS, 824 (2017), pp. 931–961.

[7] R. CHATELIN AND P. PONCET, *A parametric study of mucociliary transport by numerical simulations of 3D non-homogeneous mucus*, JOURNAL OF BIOMECHANICS, 49 (2016), pp. 1772–1780.

[8] E. Y. T. CHEN, M. GARNICA, Y.-C. WANG, C.-S. CHEN, AND W.-C. CHIN, *Mucin Secretion Induced by Titanium Dioxide Nanoparticles*, PLOS ONE, 6 (2011).

[9] E. Y. T. CHEN, Y.-C. WANG, C.-S. CHEN, AND W.-C. CHIN, *Functionalized Positive Nanoparticles Reduce Mucin Swelling and Dispersion*, PLOS ONE, 5 (2010).

[10] M. COUTANCEAU AND R. BOUARD, *Experimental determination of the main features of the viscous flow in the wake of a circular cylinder in uniform translation. part 1. steady flow*, Journal of Fluid Mechanics, 79 (1977), pp. 231–256.

[11] Y. DING, J. C. NAWROTH, M. J. MCFALL-NGAI, AND E. KANSO, *Mixing and transport by ciliary carpets: a numerical study*, JOURNAL OF FLUID MECHANICS, 743 (2014), pp. 124–140.

[12] C. EHRE, C. RIDLEY, AND D. J. THORNTON, *Cystic fibrosis: An inherited disease affecting mucin-producing organs*, INTERNATIONAL JOURNAL OF BIOCHEMISTRY & CELL BIOLOGY, 52 (2014), pp. 136–145.

[13] L. FERIANI, M. JUENET, C. J. FOWLER, N. BRUOT, M. CHIOCCIOLI, S. M. HOLLAND, C. E. BRYANT, AND P. CICUTA, *Assessing the Collective Dynamics of Motile Cilia in Cultures of Human Airway Cells by Multiscale DDM*, BIOPHYSICAL JOURNAL, 113 (2017), pp. 109–119.

[14] G. FULFORD AND J. BLAKE, *Mucociliary Transport in the Lung*, JOURNAL OF THEORETICAL BIOLOGY, 121 (1986), pp. 381–402.

[15] L. GHEBER AND Z. PRIEL, *Extraction of cilium beat parameters by the combined application of photoelectric measurements and computer simulation*, BIOPHYSICAL JOURNAL, 72 (1997), pp. 449–462.

[16] S. GUERON, K. LEVITGUREVICH, N. LIRON, AND J. BLUM, *Cilia internal mechanism and metachronal coordination as the result of hydrodynamical coupling*, PROCEEDINGS OF THE NATIONAL ACADEMY OF SCIENCES OF THE UNITED STATES OF AMERICA, 94 (1997), pp. 6001–6006.

[17] J. K. GUSTAFSSON, A. ERMUND, D. AMBORT, M. E. JOHANSSON, H. E. NILSSON, K. THORELL, H. HEBERT, H. SJÖVALL, AND G. C. HANSSON, *Bicarbonate and functional cftr channel are required for proper mucin secretion and link cystic fibrosis with its mucus phenotype*, Journal of Experimental Medicine, 209 (2012), pp. 1263–1272.

[18] J. HALL, *Simulation program git*.
`https://github.com/JonHall101/CUDA_IBLB_11`.
(Accessed on 04/09/2020).

[19] J. HALL AND N. CLARKE, *The mechanics of cilium beating: quantifying the relationship between metachronal wavelength and fluid flow rate*, Journal of Fluid Mechanics, 891 (2020), p. A20.

[20] S. HANASOGE, P. J. HESKETH, AND A. ALEXEEV, *Microfluidic pumping using artificial magnetic cilia*, MICROSYSTEMS & NANOENGINEERING, 4 (2018).

[21] S. HUSSAIN, J. A. J. VANOIRBEEK, K. LUYTS, V. DE VOOGHT, E. VERBEKEN, L. C. J. THOMASSEN, J. A. MARTENS, D. DINSDALE, S. BOLAND, F. MARANO, B. NEMERY,

AND P. H. M. HOET, *Lung exposure to nanoparticles modulates an asthmatic response in a mouse model*, EUROPEAN RESPIRATORY JOURNAL, 37 (2011), pp. 299–309.

[22] J. HUSSONG, W.-P. BREUGEM, AND J. WESTERWEEL, *A continuum model for flow induced by metachronal coordination between beating cilia*, JOURNAL OF FLUID MECHANICS, 684 (2011), pp. 137–162.

[23] I. ISPOLATOV AND M. GRANT, *Lattice Boltzmann method for viscoelastic fluids*, PHYSICAL REVIEW E, 65 (2002).

[24] P. G. JAYATHILAKE, Z. TAN, D. V. LE, H. P. LEE, AND B. C. KHOO, *Three-dimensional numerical simulations of human pulmonary cilia in the periciliary liquid layer by the immersed boundary method*, COMPUTERS & FLUIDS, 67 (2012), pp. 130–137.

[25] J. P. KEENER, S. SIRCAR, AND A. L. FOGELSON, *KINETICS OF SWELLING GELS*, SIAM JOURNAL ON APPLIED MATHEMATICS, 71 (2011), pp. 854–875.

[26] M. KESIMER, C. EHRE, K. A. BURNS, C. W. DAVIS, J. K. SHEEHAN, AND R. J. PICKLES, *Molecular organization of the mucins and glycocalyx underlying mucus transport over mucosal surfaces of the airways*, MUCOSAL IMMUNOLOGY, 6 (2013), pp. 379–392.

[27] S. N. KHADERI, J. M. J. DEN TOONDER, AND P. R. ONCK, *Microfluidic propulsion by the metachronal beating of magnetic artificial cilia: a numerical analysis*, Journal of Fluid Mechanics, 688 (2011), p. 44,Äì65.

[28] T. KRUGER ET AL., *The Lattice Boltzmann Method Principles and Practice*, Graduate Texts in Physics, 2017, pp. 653–687.

[29] P. K. KUNDU, *Fluid mechanics [electronic resource]*, Academic Press, Amsterdam ; Boston, 4th ed., 2008.

[30] S. K. LAI, Y.-Y. WANG, D. WIRTZ, AND J. HANES, *Micro- and macrorheology of mucus*, Advanced Drug Delivery Reviews, 61 (2009), pp. 86 – 100.

[31] A. LEHTINEN, A. PUISTO, X. ILLA, M. MOHTASCHEMI, AND M. ALAVA, *Transient shear banding in viscoelastic maxwell fluids*, Soft Matter, 9 (2013), pp. 8041–8049.

[32] Z. LI, J. FAVIER, U. D'ORTONA, AND S. PONCET, *An immersed boundary-lattice Boltzmann method for single- and multi-component fluid flows*, JOURNAL OF COMPUTATIONAL PHYSICS, 304 (2016), pp. 424–440.

[33] H. MACHEMER, *Ciliary activity and the origin of metachrony in paramecium: Effects of increased viscosity*, Journal of Experimental Biology, 57 (1972), pp. 239–259.

[34] S. M. MITRAN, *Metachronal wave formation in a model of pulmonary cilia*, COMPUTERS & STRUCTURES, 85 (2007), pp. 763–774.

[35] NVIDIA, *Visual profiler*. `https://developer.nvidia.com/nvidia-visual-profiler`. (Accessed on 09/04/2020).

[36] A. PINELLI, I. Z. NAQAVI, U. PIOMELLI, AND J. FAVIER, *Immersed-boundary methods for general finite-difference and finite-volume Navier-Stokes solvers*, JOURNAL OF COMPUTATIONAL PHYSICS, 229 (2010), pp. 9073–9091.

[37] D. ROGERS, *Airway mucus hypersecretion in asthma: an undervalued pathology?*, CURRENT OPINION IN PHARMACOLOGY, 4 (2004), pp. 241–250.

[38] D. ROGERS AND T. EVANS, *PLASMA EXUDATION AND EDEMA IN ASTHMA*, BRITISH MEDICAL BULLETIN, 48 (1992), pp. 120–134.

[39] P. SATIR, *Studies on cilia*, The Journal of Cell Biology, 18 (1963), pp. 345–365.

[40] P. SATIR, T. HEUSER, AND W. S. SALE, *A structural basis for how motile cilia beat*, BioScience, 64 (2014), p. 1073.

[41] M. H. SEDAGHAT, M. M. SHAHMARDAN, M. NOROUZI, P. G. JAYATHILAKE, AND M. NAZARI, *Numerical simulation of muco-ciliary clearance: immersed boundary lattice Boltzmann method*, COMPUTERS & FLUIDS, 131 (2016), pp. 91–101.

[42] S. SHIMURA, Y. ANDOH, M. HARAGUCHI, AND K. SHIRATO, *Continuity of airway goblet cells and intraluminal mucus in the airways of patients with bronchial asthma*, EUROPEAN RESPIRATORY JOURNAL, 9 (1996), pp. 1395–1401.

[43] S. SIRCAR AND A. ROBERTS, *ION MEDIATED CROSSLINK DRIVEN MUCOUS SWELLING KINETICS*, DISCRETE AND CONTINUOUS DYNAMICAL SYSTEMS-SERIES B, 21 (2016), pp. 1937–1951.

[44] D. J. SMITH, E. GAFFNEY, AND J. R. BLAKE, *Modelling mucociliary clearance*, RESPIRATORY PHYSIOLOGY & NEUROBIOLOGY, 163 (2008), pp. 178–188.

[45] D. J. SMITH, E. A. GAFFNEY, AND J. BLAKE, *Mathematical modelling of cilia-driven transport of biological fluids*, PROCEEDINGS OF THE ROYAL SOCIETY A-MATHEMATICAL PHYSICAL AND ENGINEERING SCIENCES, 465 (2009), pp. 2417–2439.

[46] D. J. SMITH, E. A. GAFFNEY, AND J. R. BLAKE, *A viscoelastic traction layer model of muco-ciliary transport*, BULLETIN OF MATHEMATICAL BIOLOGY, 69 (2007), pp. 289–327.

[47] P. VERDUGO, *Hydration Kinetics of Exocytosed Mucins In Cultured Secretory-Cells Of The Rabbit Trachea - A New Model*, CIBA FOUNDATION SYMPOSIA, 109 (1984), pp. 212–225.

[48] E. M. VIGGEN, *The Lattice Boltzmann Method with Applications in Acoustics*, Masters Thesis, NTNU, (2009).

[49] D. WARHEIT, T. WEBB, C. SAYES, V. COLVIN, AND K. REED, *Pulmonary instillation studies with nanoscale TiO2 rods and dots in rats: Toxicity is not dependent upon particle size and surface area*, TOXICOLOGICAL SCIENCES, 91 (2006), pp. 227–236.

[50] J. WIDDICOMBE AND J. WIDDICOMBE, *Regulation of Human Airway Surface Liquid*, RESPIRATION PHYSIOLOGY, 99 (1995), pp. 3–12.

[51] X. YANG, R. H. DILLON, AND L. J. FAUCI, *An integrative computational model of multiciliary beating*, BULLETIN OF MATHEMATICAL BIOLOGY, 70 (2008), pp. 1192–1215.

[52] Q. ZOU AND X. HE, *On pressure and velocity boundary conditions for the lattice Boltzmann BGK model*, PHYSICS OF FLUIDS, 9 (1997), pp. 1591–1598.